Electronic Supplementary Information for

Tetrathiafulvalene (TTF) Derivatives as Catholytes for Dual-Type Redox Flow Batteries:

Molecular Engineering Enables High Energy Density and Cyclability

Xiao Wang,[a,‡] Amir Lashgari,[a,‡] Rabin Siwakoti,[a] Rajeev K Gautam,[a] Jack J. McGrath,[a] Prasenjit Sarkar,[a] Grace Naber,[a] Jingchao Chai,[a] Jianbing "Jimmy" Jiang[a,*]

[a]Department of Chemistry, University of Cincinnati, P.O. Box 210172, Cincinnati, Ohio 45221-0172, United States.

*Corresponding author: jianbing.jiang@uc.edu

‡Equal contribution

Table of Content

Contents	Page

Experimental Section

General methods. All chemicals were purchased from Sigma-Aldrich, stored in an argon-filled glovebox and used without further purification. The perfluorosulfonic acid ion-exchange membrane was purchased from Dongyuechem Corporation, China. The NMR analysis was performed at room temperature using a Bruker AV 400 MHz spectrometer. The unit of chemical shifts is based on ppm. All CV data were collected on a Bio-Logic potentiostat. SEM and EDS imagines were obtained on Hitachi SU8230 UHR Cold Field Emission (CFE) SEM. **TTF** was purchased and used without further purification. HR-MS analysis was performed on an Orbitrap Fusion Lumos mass spectrometer from Thermo Scientific.

Cyclic voltammetry. For homogeneous CV measurements for **TTF** compounds, a 3-mm glassy carbon was used as the working electrode, and was polished with 50 nm Al_2O_3 prior to measurements. Platinum wire (0.5 mm) was used as the counter electrodes, $Ag/AgNO_3$ or $Ag/AgCl$ electrode was used as a reference electrode. For heterogeneous CV measurements for **TTF**, carbon paper was used as the working electrode. Platinum wire (0.5 mm) was used as the counter electrodes a $Ag/AgCl$ electrode was used reference electrode. **TTF** or **CN-TTF** was dispersed in CH_2Cl_2 (10 mg/mL) and sonicated for 5 min, and then drop-casted on a carbon paper and dried in an oven. For measurements in nonaqueous tests, a $Ag/AgNO_3$ reference electrode was used with Fc/Fc^+ as reference standard. The scan rate is 50 mV/s. For CV test of extract solution, the **TTF** or **CN-TTF**/KB suspension electrolytes were dried at 60 °C for 12 h. Then, 1.0 mg of dried **TTF** or **CN-TTF**/KB electrolytes were soaked in 1.0 mL DMSO for 2.0 h to get clear supernatant liquid. 0.1 M tetrabutylammonium hexafluorophosphate was used as the supporting salt.

Calculation of diffusion coefficient and electron transfer rate. Linear sweep voltammetry (LSV) studies were carried out using a Pine modulated speed rotator with Biologic

potentiostats. Rotating disk electrode (RDE, diameter: 5 mm), Pt wire electrode and Ag/AgNO$_3$ electrode were used as the working, counter and reference electrodes, respectively. Before testing, the samples were purged with argon for 10 min to remove dioxygen. The electrochemical kinetics of **TTF**, **CN-TTF** in 0.1 M TBAPF$_6$/PC, **PEG3-TTF** in 1 M Li hexafluorophosphate (LiPF$_6$)/ethylene carbonate (EC)/ethyl methyl carbonate (EMC), and 0.1 M TBAPF$_6$/MeCN were studied using a RDE. LSV dates were collected at different rotation rates ranging from 100 to 2500 rpm. The diffusion coefficient (D) of electroactive materials was calculated from the Lévich plot:[S1-3]

$$i = 0.620nFAC_0D^{2/3}\omega^{1/2}\upsilon^{-1/6} \qquad \text{Equation S1}$$

Where i is limiting current density, n is the number of electrons in redox process, F is Faraday's constant, A is the area of the glassy carbon electrode, C$_0$ is the concentration of active material, ω is angular rotation rate and υ is the kinematic viscosity of 0.1 M TBAPF$_6$-PC/ 0.1 M TBAPF$_6$-MeCN/ 0.1 M LiPF$_6$ EC DEC.

The kinetic rate constant is calculated by Equation 2: [S4]

$$i_0 = FAC_0k_0 \qquad \text{Equation S2}$$

Where i$_0$ was calculated from fitting line of Butler-Volmer equation, x-intercept is the log of the exchange current i$_0$ (0.0003 A), F is Faraday's constant, A is the area of the glassy carbon electrode (0.196 cm^2), C$_0$ is the concentration of redoxmers (1×10^{-6} mol/cm^3), k$_0$ is reaction rate constant (cm/s).

SEM measurements. The tests were performed using an energy X-ray spectroscopy mode. The **TTF**/KB slurry was directly dried on double-sided carbon tape before it was sputter coated with gold to improve imaging. EDS was conducted to obtain information on the C, N, S

compositions of the samples. For membrane tests, the membranes before and after cycling were washed by EMC for three times and dried for 1 h in oven, then dried on double-sided carbon tape before it was sputter coated with gold to improve imaging. EDS was conducted to obtain information on the S compositions of the samples.

Preparation of slurry catholyte. For the slurry catholyte, a sample of 0.5 M **TTF** or **CN-TTF** with 40 g/L Ketjen carbon(KB) was prepared following this procedure: Firstly, 51 mg **TTF** or 136 mg **CN-TTF** were mixed with 20 mg KB and ground for 0.5 h to afford a uniform mixture. Then, 0.5 mL 2 M LiTFSI/H_2O solution (for **TTF** is 2 M LiTFSI in 95/5 H_2O/TEGDME) was added into the powder mixture, and the resultant mixture was ground for 0.5 h (ignoring the volume change after mixing solids and liquids). Please note that the concentration description in this wrok ignores the volume change from the soild materials.

Battery measurements. The slurry battery setup is composed of two polytetrafluoroethylene plates, two copper plates, two graphite current collectors, two rubber frames, and graphite felt and carbon paper electrodes with an active area of 1 cm^2. Perfluorosulfonic acid ion-exchange membrane was sandwiched between graphite felt and carbon paper with pretreatment of presoaking in 2 M LiTFSI overnight. All battery measurements were conducted on a Bio-Logic potentiostat. For **TTF** battery tests, Zn plate and 0.5 M **TTF** in 2 M LiTFSI in 95/5 H_2O/TEGDME were used as anolyte and catholyte, respectively. For **CN-TTF** battery tests, Zn plate and 0.5 M, 1.0 M, and 1.5 M **CN-TTF** in 2 M LiTFSI/H_2O was used as anolyte and catholyte, respectively. When assembling the battery, the battery chamber (1 x 1 x 0.5 cm^3) was filled with the slurry. A perfluorosulfonic acid ion-exchange membrane was used as the battery separator.

The device for the **V-TFSI/PEG3-TTF** battery was composed of two aluminum alloy plates, two polytetrafluoroethylene plates, two copper plates, graphite current collector, polytetrafluoroethylene frame, and graphite felt electrodes with an active area of 5 cm^2. Daramic® 175 membrane was sandwiched between two graphite felts without pretreatment. For single electron RFB study, 0.1 M **PEG3-TTF** and 0.12 M **V-TFSI** in 0.5 M TBAPF$_6$/MeCN (6 mL) was used as both the anolyte and catholyte. For the double electron RFB study, 0.1 M **PEG3-TTF** and 0.24 M **V-TFSI** in 0.5 M TBAPF$_6$/MeCN (5 mL) was employed as both the anolyte and catholyte.

The solution RFBs of Li/**PEG3-TTF** were composed of polytetrafluoroethylene plate, graphite current collector, polytetrafluoroethylene frame, and graphite felt electrodes with an active area of 8 cm^2. Daramic® 175 membrane and Fumasep® PK FAB 130 were sandwiched between two graphite felts. The Fumasep® PK FAB 130 was pretreatment by soaking in1 M LiPF$_6$ EC EMC solution overnight. All battery measurements were conducted on a Bio-Logic VSP potentiostat with a flow rate of 15 mL/min. A 2.5 mL 0.1/0.3/0.5 M **PEG3-TTF**/1 M LiPF$_6$ EC EMC (v 1:1 with 2% FEC and 1% VC) solution and Li metal in 4 mL 1 M LiPF$_6$ EC/EMC (v 1:1 with 2% FEC and 1% VC) were used as catholyte and anode, respectively.

The impendence of the battery was conducted using electrochemical impedance spectroscopy (EIS) with frequencies ranging from 100 mHz to 200 kHz if there is no special instruction. The impendence of the the slurry on working electrode in a three-electrode system (working electrode: carbon paper deposited with active material and KB; reference electrode: Ag/AgNO$_3$; counter electrode: Platinum wire) was conducted at a frequency range of 50 mHz–1 MHz.

Calculation of energy density

The energy density of Li-andoe RFB was calculated from the following equation:[S5]

Energy Density (Wh/L) = nCFV/3600   Equation S3

where F is the Faraday constant, n is the number of electrons transferred during reaction per mole reactant, C is the concentration of redoxmer solution, V is the battery's voltage.

The actual energy density of RFB was obtained by following equation:

Actual Energy Density (Wh/L) = Q_hV/Vo   Equation S4

where Q_h is the highest discharge capacity, V is the battery's voltage, Vo is the volume of electrolyte.

The energy density of the two side solution battery wree calculated according to Equation S4,[S6] where n is the number of electrons involved in the cell reaction, C is the concentration of active materials, F is Faraday's constant, V is the cell voltage, and μ is the factor that represents the overall volumes of anolyte and catholyte (μ = 1 + (max solubility; less soluble electrolyte)/(max solubility; more soluble electrolyte)):

Energy density (Wh/L) = nCFV/μ   Equation S5

Synthesis

Compounds **CN-TTF**[S7] and **PEG3-TTF**[S8,9] were synthesized according to reported procedures. Compound **PEG1-TTF** was synthesized here using a different synthetic route from the reported one.[S10] Scheme S1 shows the synthesis procedure of **PEG1-TTF**.

Synthesis of Compound 2. A sample of K_2CO_3 (2.01 g, 14.6 mmol, 2.20 eq) was added to the solution of **1**[S11] (2.69 g, 6.62 mmol, 1.00 eq) in MeOH (140 mL) and refluxed under Ar for 1 h. After cooling the solution to 40 ºC, 2-methoxyethyl chloride (4.84 mL, 53.0 mmol, 8.00 eq) was added to the mixture and refluxed under argon for 12 h. After removing the solvent by a rotary evaporator, the crude mixture was washed with 10% HCl aqueous solution and extracted with

CH$_2$Cl$_2$. The organic extract was combined and dried over Na$_2$SO$_4$. The solution was dried by a rotary evaporator. The crude residue was purified by column chromatography (SiO$_2$; 10-20% ethyl acetate in CH$_2$Cl$_2$). Yield: 1.26 g, 61%. ^{1}H NMR (400 MHz, CDCl$_3$), δ 3.60 (t, 4H, J = 8 Hz), 3.37 (s, 6H); 3.06 (t, 4H, J = 8 Hz); ^{13}C NMR (100 MHz, CDCl$_3$), δ 36.16, 58.89, 70.86, 136.61, 211.12; HR-MS obsd 336.94893, calcd 336.94895 [M + Na$^+$, M = C$_9$H$_{14}$O$_2$S$_5$].

Synthesis of Compound 3. A solution of Hg(OAc)$_2$ (1.50 g, 4.71 mmol, 1.50 eq) in CH$_3$COOH (8.00 mL) was added to the solution of **2** (0.990 g, 3.14 mmol, 1.00 eq) in CHCl$_3$ (24.0 mL) and stirred under argon at 40 ºC for 12 h. The solution was washed three times with saturated NaHCO$_3$ and brine and extracted with CH$_2$Cl$_2$. The organic extract was combined and dried over Na$_2$SO$_4$. The solution was filtered, and the filtrate was dried via a rotary evaporator. The crude residue was purified by column chromatography (SiO$_2$; 10-20% ethyl acetate in CH$_2$Cl$_2$). Yield: 0.850 g, 91%. ^{1}H NMR (400 MHz, CDCl$_3$), δ 3.61 (t, 4H, J = 8 Hz), 3.37 (s, 6H); 3.04 (t, 4H, J = 8 Hz); ^{13}C NMR (100 MHz, CDCl$_3$), δ 36.01, 58.87, 70.93, 127.56, 189.59; HR-MS obsd 320.97187, calcd 320.97180 [M + Na$^+$, M = C$_9$H$_{14}$O$_3$S$_4$].

Synthesis of Compound PEG1-TTF.[S10] A sample of P(OEt)$_3$ (2.62 mL, 15.2 mmol, 5.40 eq) was added to **3** (0.850 g, 2.83 mmol, 1.00 eq) and stirred at 100 ºC for 1 hour. CH$_2$Cl$_2$ was used to dissolve the crude compound, and the crude solution was loaded onto the column chromatography (SiO$_2$; 30-50% ethyl acetate in CH$_2$Cl$_2$) for purification. Yield: 0.390 g, 49%. ^{1}H NMR (400 MHz, CDCl$_3$), δ 3.57 (t, 8H, J = 8 Hz), 3.37 (s, 12H); 2.99 (t, 8H, J = 8 Hz); ^{13}C NMR (100 MHz, CDCl$_3$), δ 35.48, 58.83, 71.11, 110.36, 127.94; HR-MS obsd 586.96444, calcd 586.96455 [M + Na$^+$, M = C$_{18}$H$_{28}$O$_4$S$_8$].
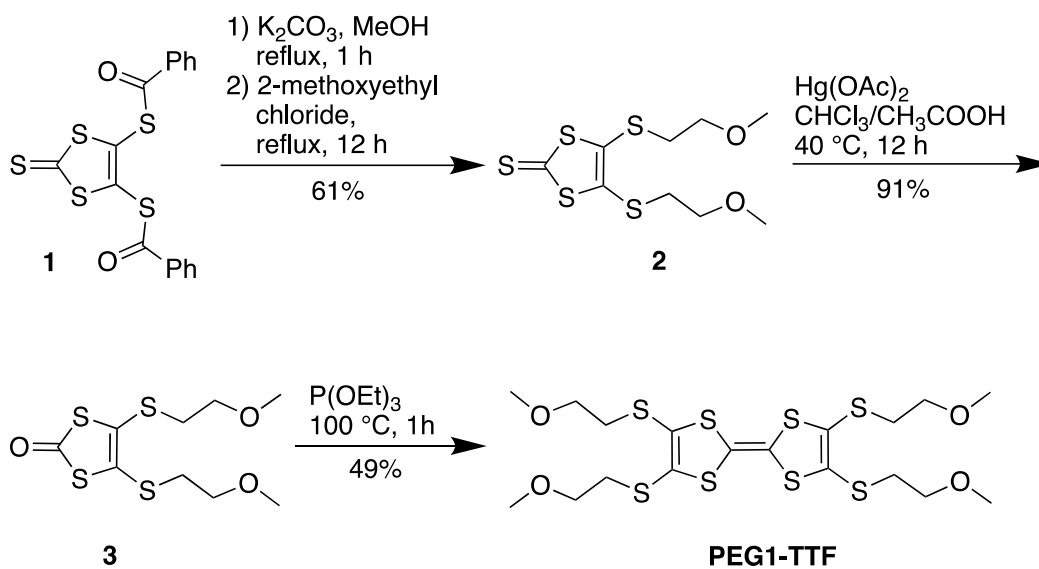
Scheme S1. Synthesis of **PEG1-TTF**.

Table S1. Solubility of **TTF** compounds in different solvents.

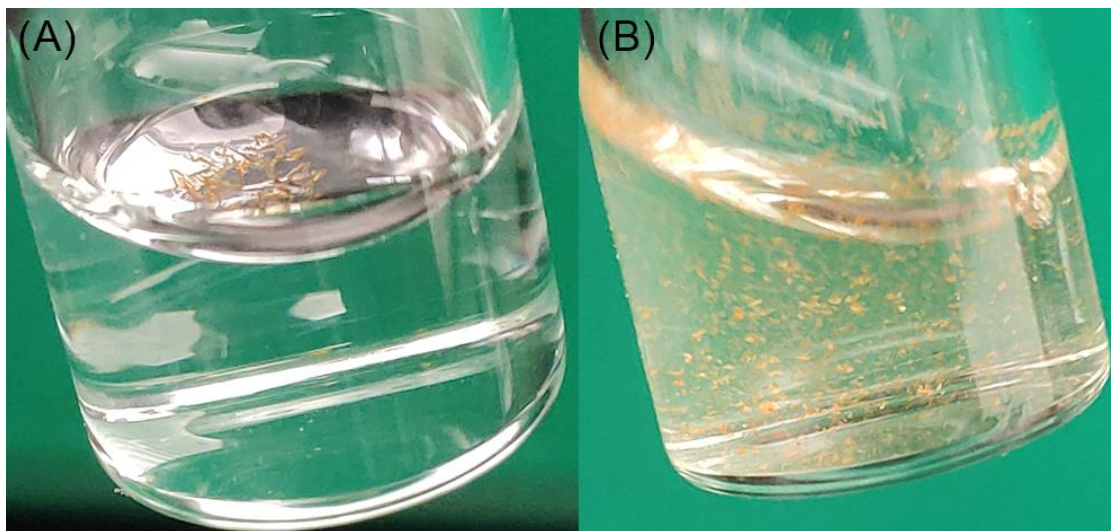|	TTF	PEG1-TTF	PEG3-TTF	CN-TTF
water	Not soluble	Not soluble	Not soluble	Not soluble
PC	0.23 M	0.35 M	Miscible	25 mM
MeCN	0.1 M	0.27 M	Miscible	~1 mM

PC: Propylene carbonate

Figure S1. Photographs of (A) **TTF** and (B) **CN-TTF** in water. Condition: ultrasonicated for 3 mins, followed by standing for 1min.
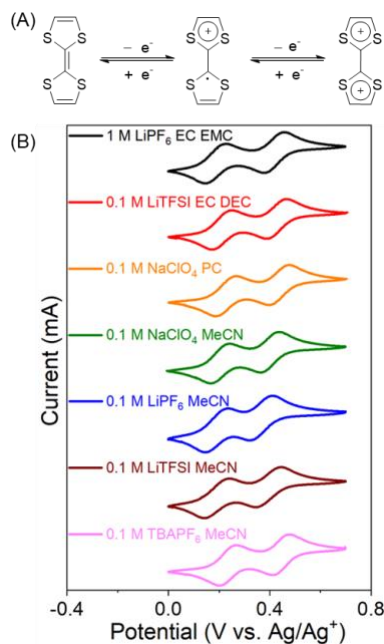
Figure S2. (A) Redox reactions of **TTF**. (B) Cyclic voltammograms for 5 mM **PEG3-TTF** compounds in different electrolytes. Scan rate: 50 mV/s
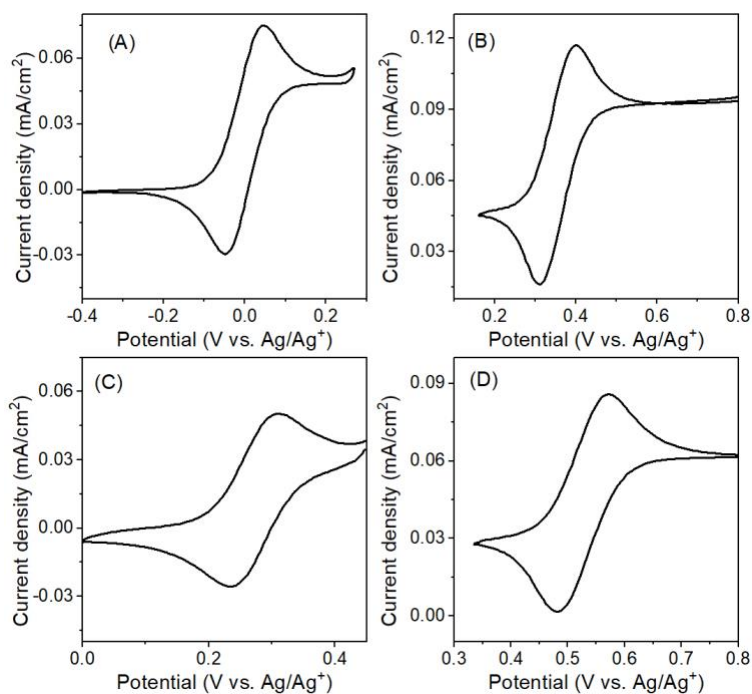

Figure S3. Cyclic voltammograms of 1 mM of (A) **TTF** first electron, (B) **TTF** second electron, (C) **CN-TTF** first electron, and (D) **CN-TTF** second electron in 0.1 M TBAPF$_6$/PC. Scan rate: 5 mV/s.

Table S2. Peak separation and peak current ratio of **TTF** and **CN-TTF** in 0.1 M TBAPF$_6$/PC.

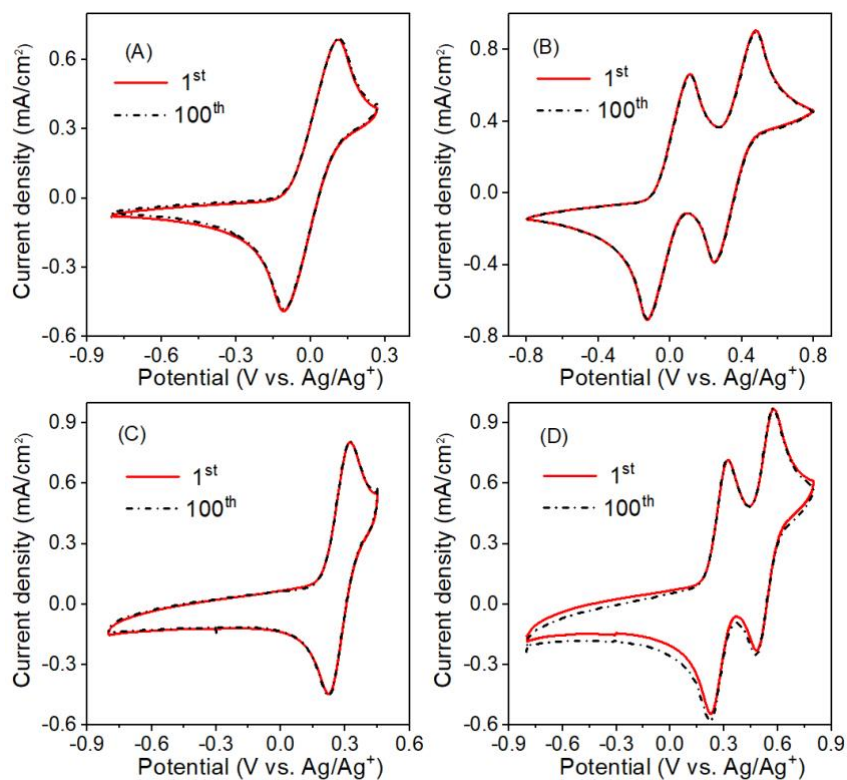|	Peak separation (mV)	Peak current ratio ($i_{p,ox}/i_{p,red}$) at 5 mV/s
1st TTF oxidation	97	1.07
2nd TTF oxidation	88	1.02
1st CN-TTF oxidation	73	1.01
2nd CN-TTF oxidation	82	1.05

Figure S4. Repeated cyclic voltammograms of 5 mM of (A) **TTF** single electron, (B) **TTF** double electron, (C) **CN-TTF** single electron, and (D) **CN-TTF** double electron before and after 100 cycles in 0.1 M TBAPF$_6$/PC. Scan rate: 50 mV/s.
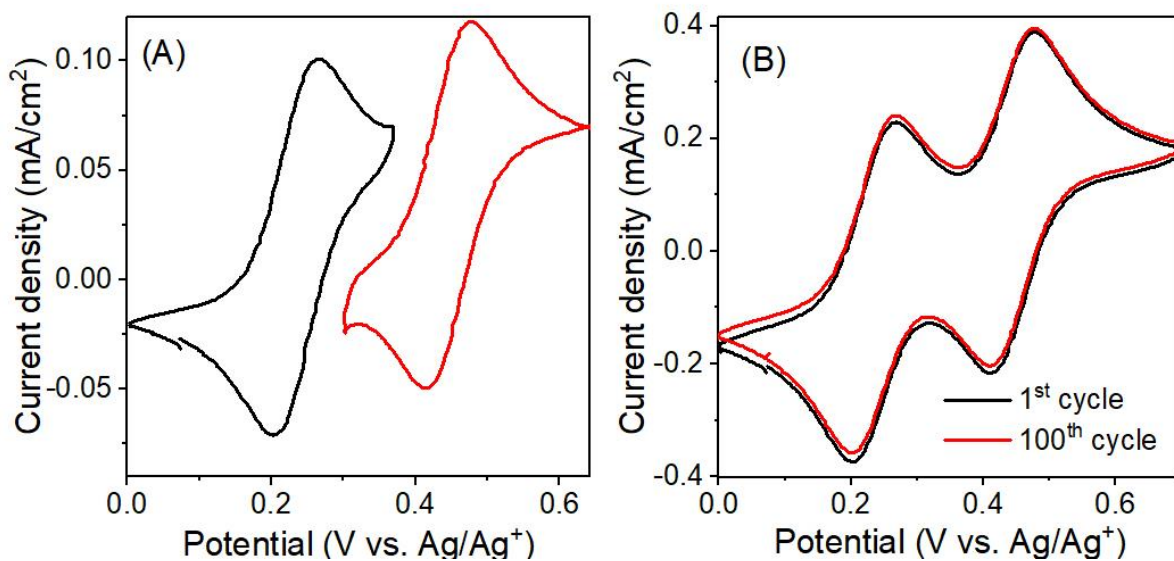
Figure S5. Cyclic voltammograms of **PEG3-TTF** in 1 M LiPF$_6$ EC/EMC. (A) scan rate: 5 mV/s, (B) comparison of 1st and 100th cycles.
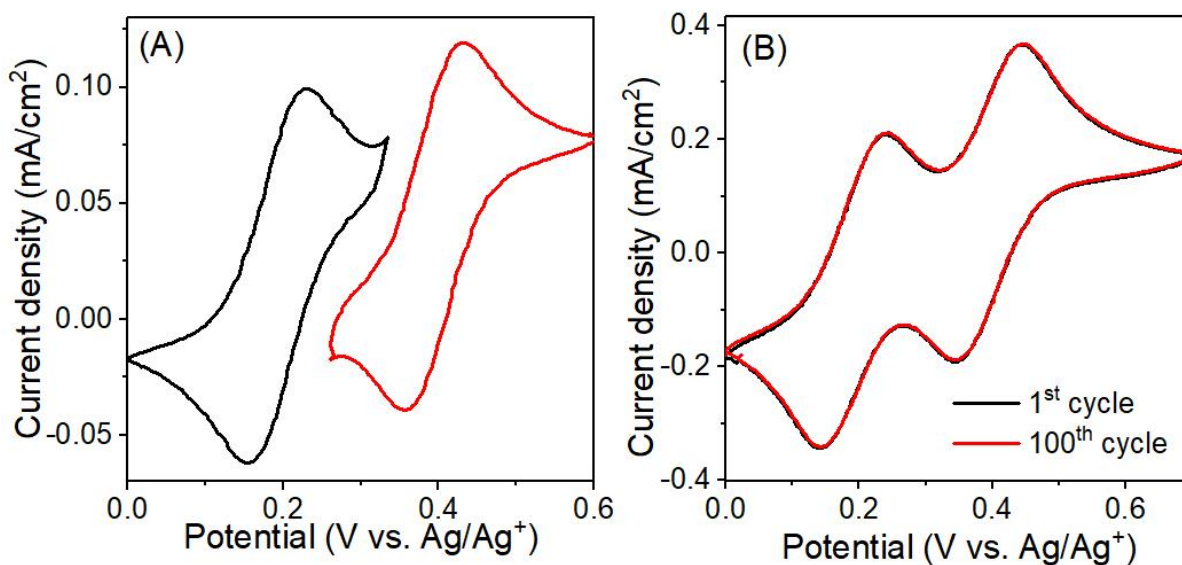

Figure S6. Cyclic voltammograms of **PEG3-TTF** in 0.1 M LiTFSI EC/DEC. (A) scan rate: 5 mV/s, (B) comparison of 1st and 100th cycles.

Figure S7. Cyclic voltammograms of **PEG3-TTF** in 0.1 M NaClO$_4$ PC. (A) scan rate: 5 mV/s, (B) comparison of 1st and 100th cycles.

Figure S8. Cyclic voltammograms of **PEG3-TTF** in 0.1 M NaClO$_4$ MeCN. (A) scan rate: 5 mV/s, (B) comparison of 1st and 100th cycles.

Figure S9. Cyclic voltammograms of **PEG3-TTF** in 0.1 M LiPF$_6$ MeCN. (A) scan rate: 5 mV/s, (B) comparison of 1st and 100th cycles.

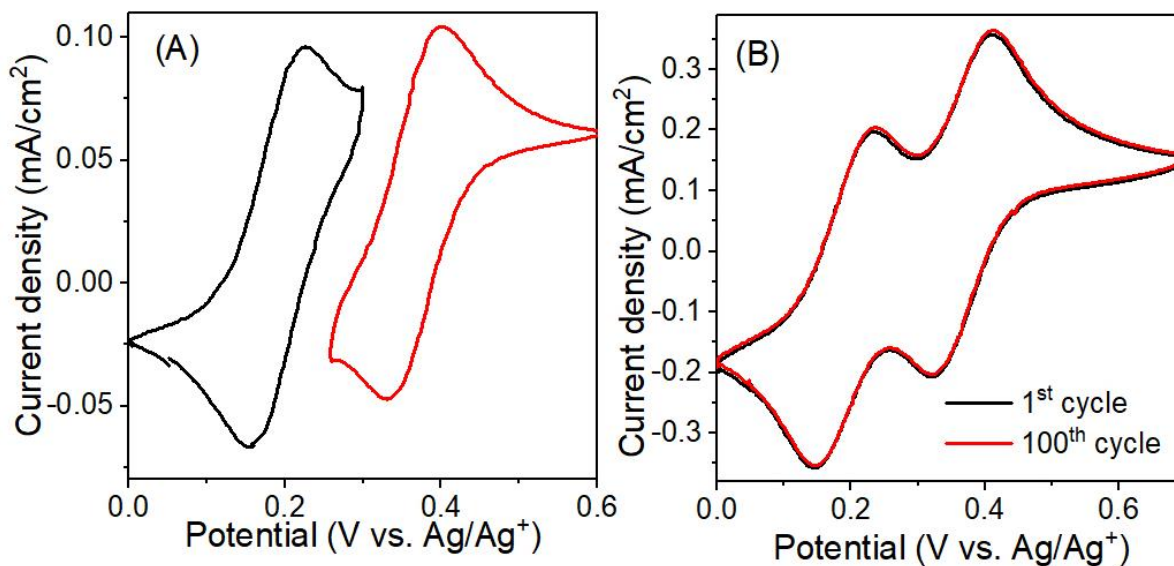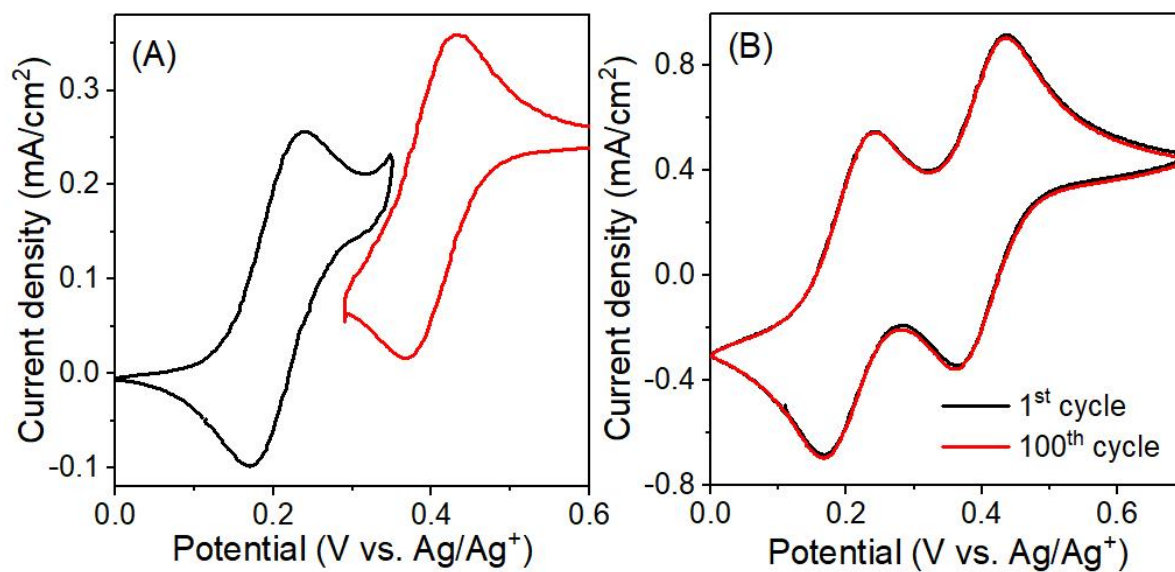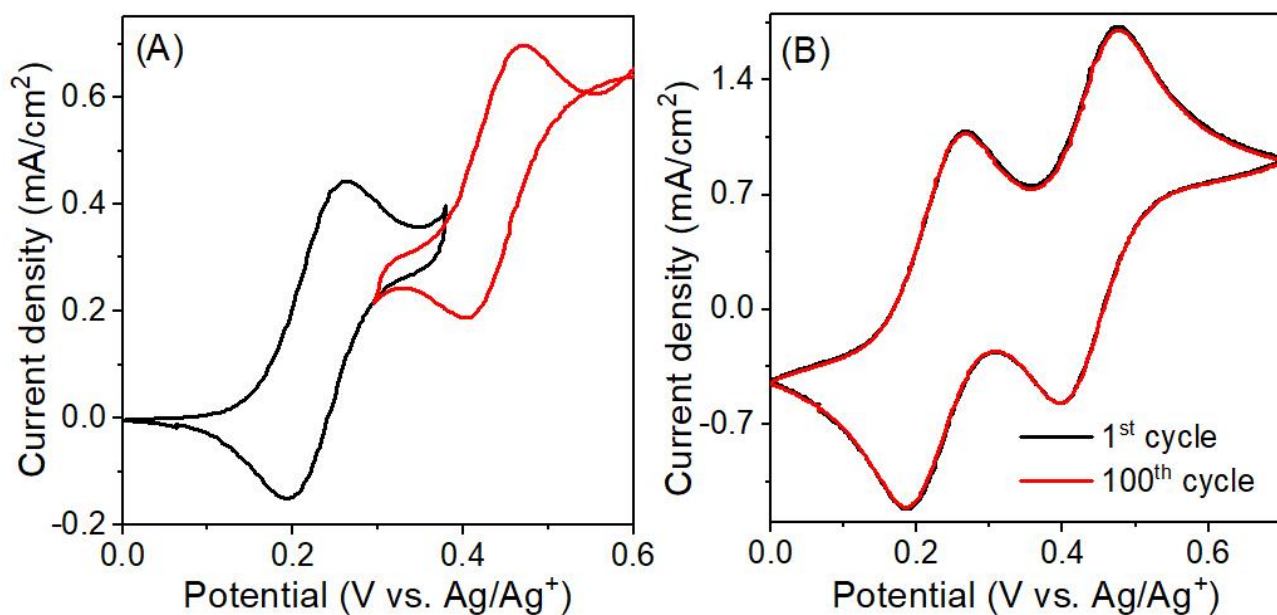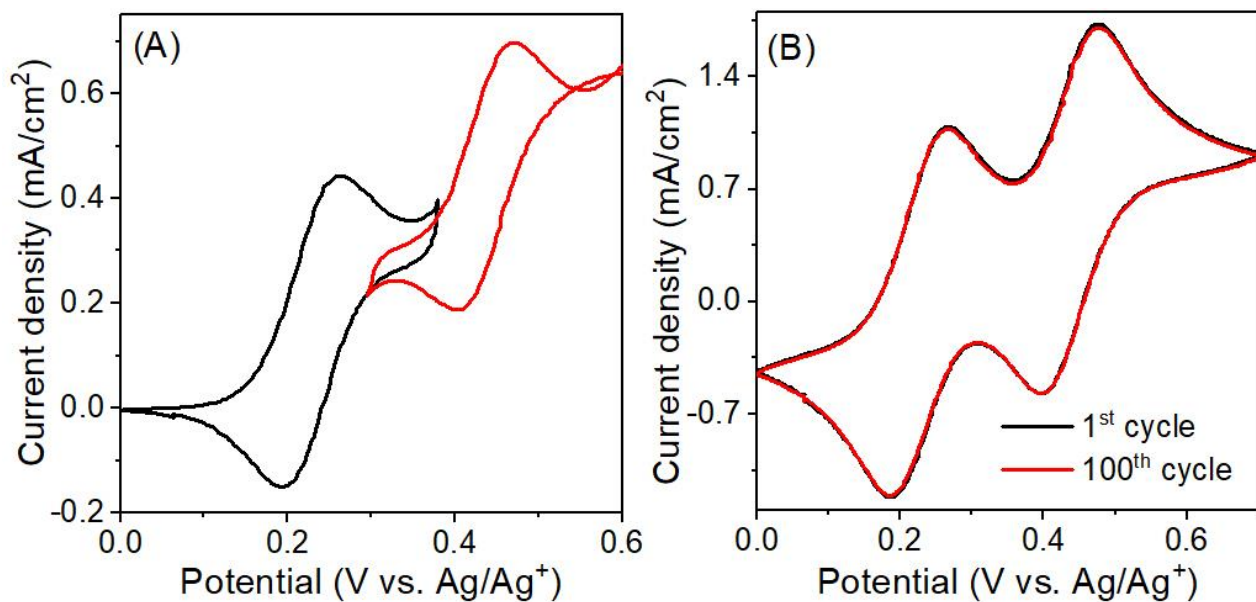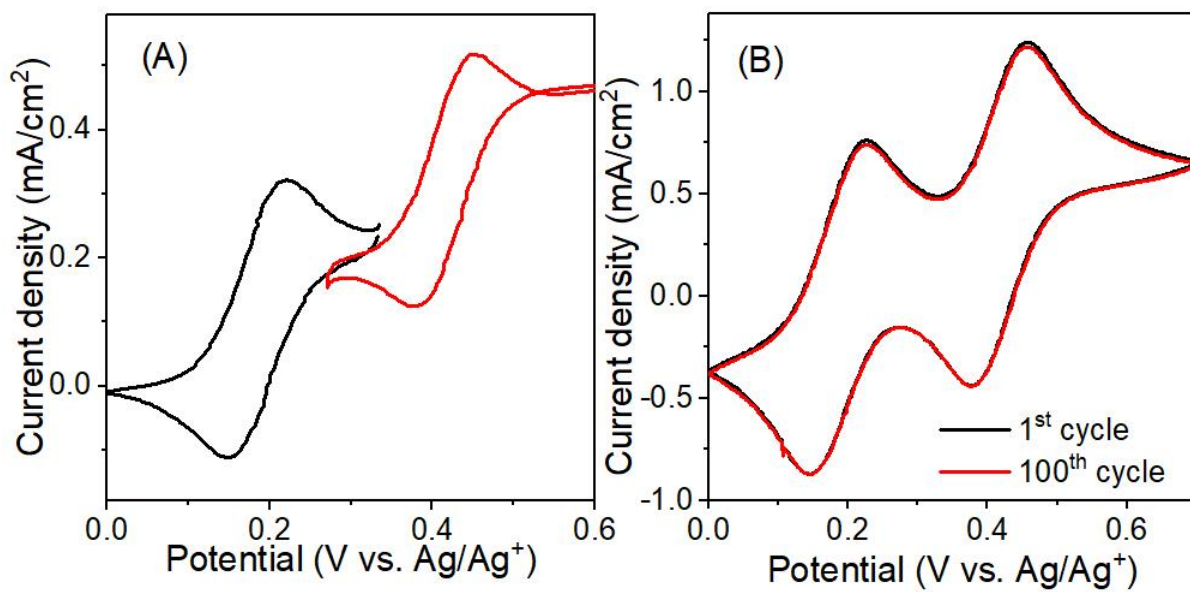**Figure S10.** Cyclic voltammograms of **PEG3-TTF** in 0.1 M LiTFSI MeCN. (A) scan rate: 5 mV/s, (B) comparison of 1st and 100th cycles.

Figure S11. Cyclic voltammograms of **PEG3-TTF** in 0.1 M TBAPF$_6$ MeCN. (A) scan rate: 5 mV/s, (B) comparison of 1st and 100th cycles.

Table S3. Summary of the electrochemical properties of **PEG3-TTF**.

Electrolyte	E_0 of first e^- (V)[a]	ΔE^b of first e^- (mV)	$(i_{p,ox}/i_{p,red})^c$ of first e^-	E_0 of second e^- (V)	ΔE of second e^- (mV)	$(i_{p,ox}/i_{p,red})$ of second e^-
1 M LiPF$_6$ EC EMC	0.24	64	1.02	0.44	65	1.02
0.1 M LiTFSI EC DEC	0.19	69	1.07	0.40	63	0.98
0.1 M NaClO$_4$ PC	0.19	70	0.98	0.37	69	1.06
0.1 M NaClO$_4$ MeCN	0.21	66	1.03	0.41	65	0.96
0.1 M LiPF$_6$ MeCN	0.23	69	1.08	0.44	63	1.05
0.1 M LiTFSI MeCN	0.20	67	0.97	0.40	63	1.01
0.1 M TBAPF$_6$ MeCN	0.19	72	1.01	0.42	68	0.99

[a]Redox potential vs. Ag/Ag$^+$
[b]Peak separation at 5 mV/s
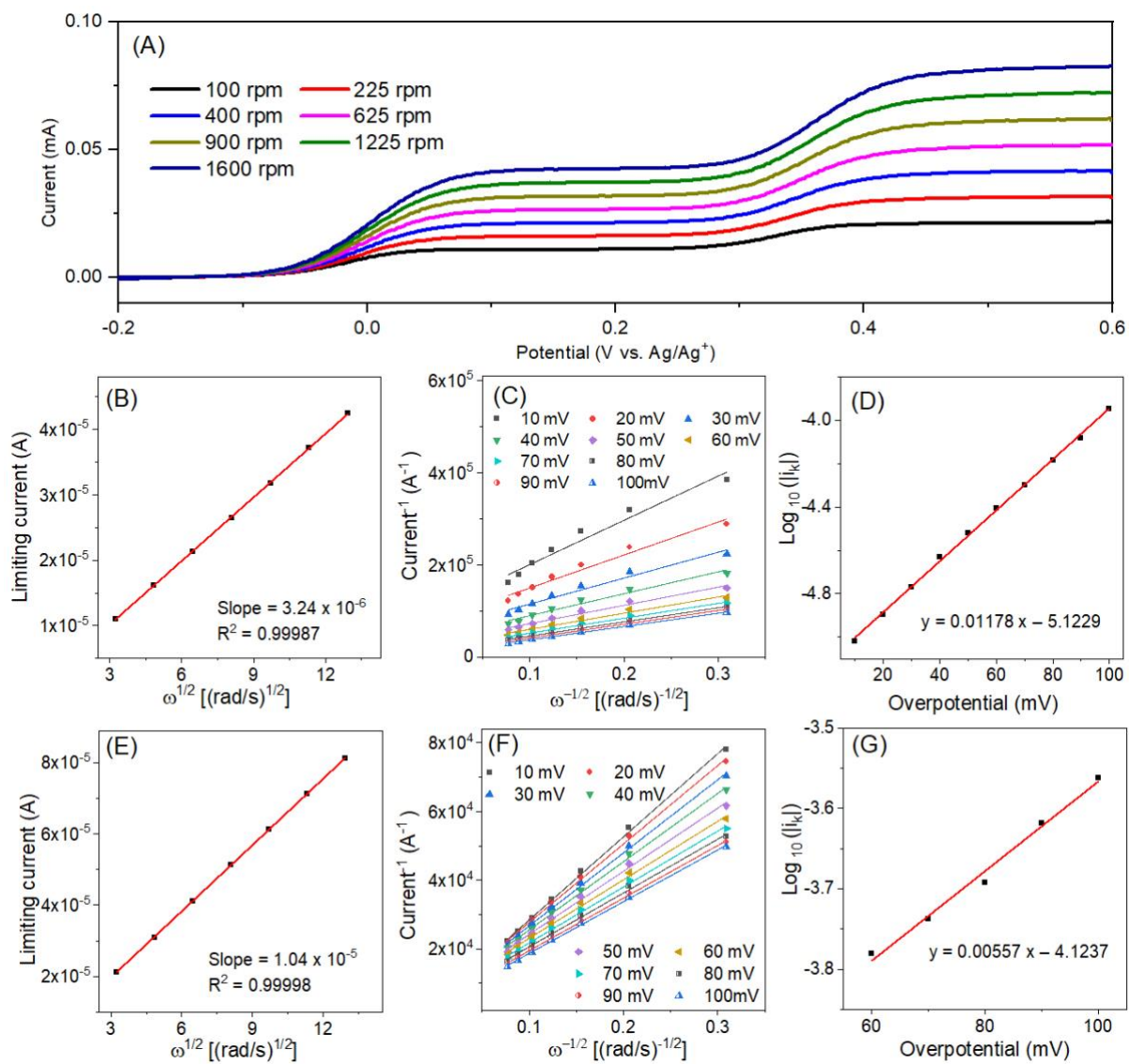[c]Peak current ratio at 5 mV

Figure S12. (A) Linear sweep voltammetry plots obtained at different rotation rates of the rotating disk electrode. (B) Peak oxidation and reduction current density versus square root of angular velocity of first electron. (C) Koutecký-Levich curve (current^{-1} vs $\omega^{-1/2}$) at different reduction overpotentials of first electron. (D) Tafel plot constructed using the current response and overpotentials of first electron. (E) Peak oxidation and reduction current density versus square root of angular velocity of second electron. (F) Koutecký-Levich curve (current^{-1} vs $\omega^{-1/2}$) at different reduction overpotentials of second electron. (G) Tafel plot constructed using the current response and overpotentials of second electron. Solution: 1 mM **TTF** in a 0.1 M TBAPF$_6$/PC electrolyte.
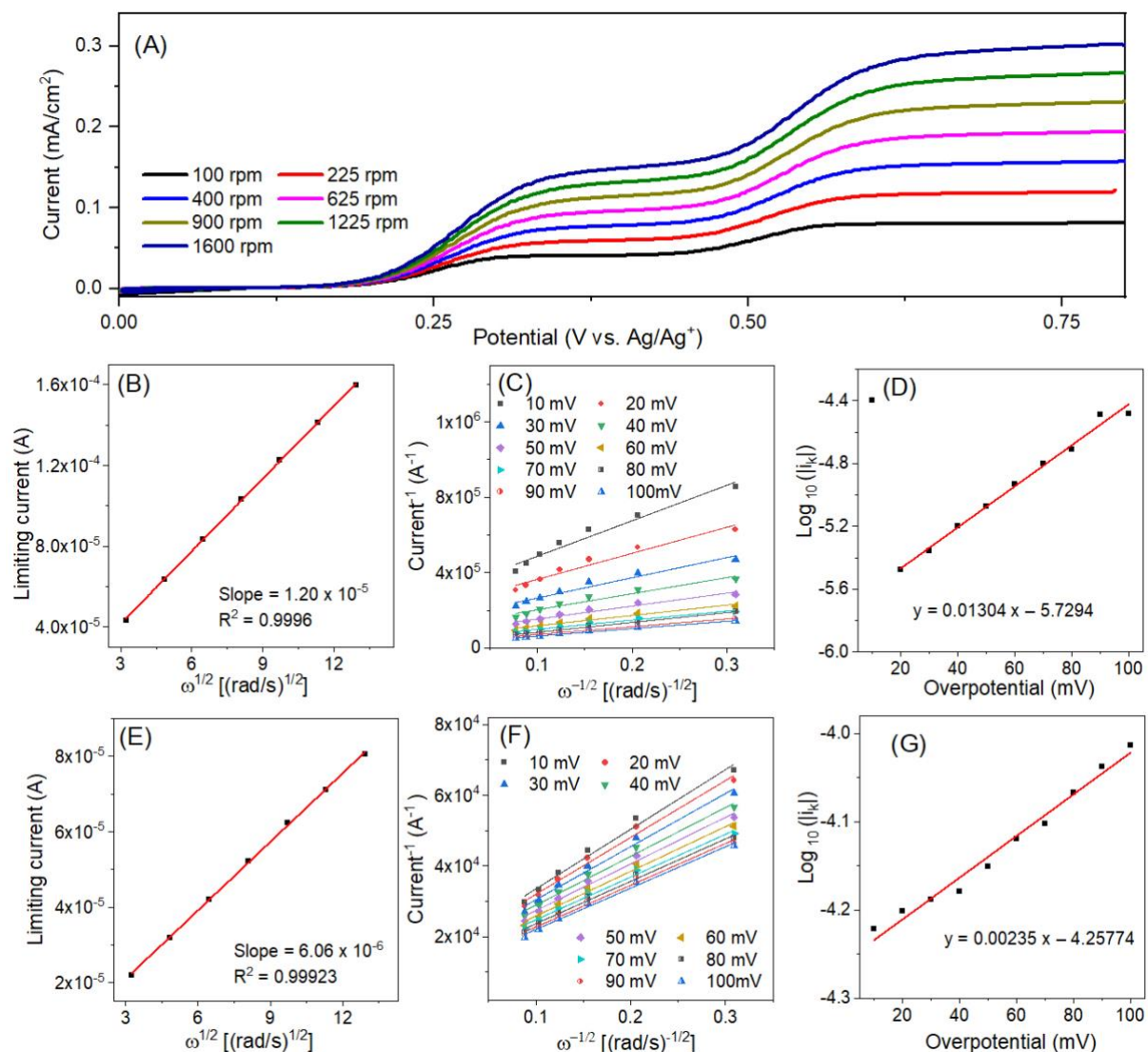
Figure S13. (A) Linear sweep voltammetry plots obtained at different rotation rates of the rotating disk electrode. (B) Peak oxidation and reduction current density versus square root of angular velocity of first electron. (C) Koutecký-Levich curve (current^{-1} vs $\omega^{-1/2}$) at different reduction overpotentials of first electron. (D) Tafel plot constructed using the current response and overpotentials of first electron. (E) Peak oxidation and reduction current density versus square root of angular velocity of second electron. (F) Koutecký-Levich curve (current^{-1} vs $\omega^{-1/2}$) at different reduction overpotentials of second electron. (G) Tafel plot constructed using the current response and overpotentials of second electron. Solution: 1 mM **CN-TTF** in a 0.1 M TBAPF$_6$/PC solution.
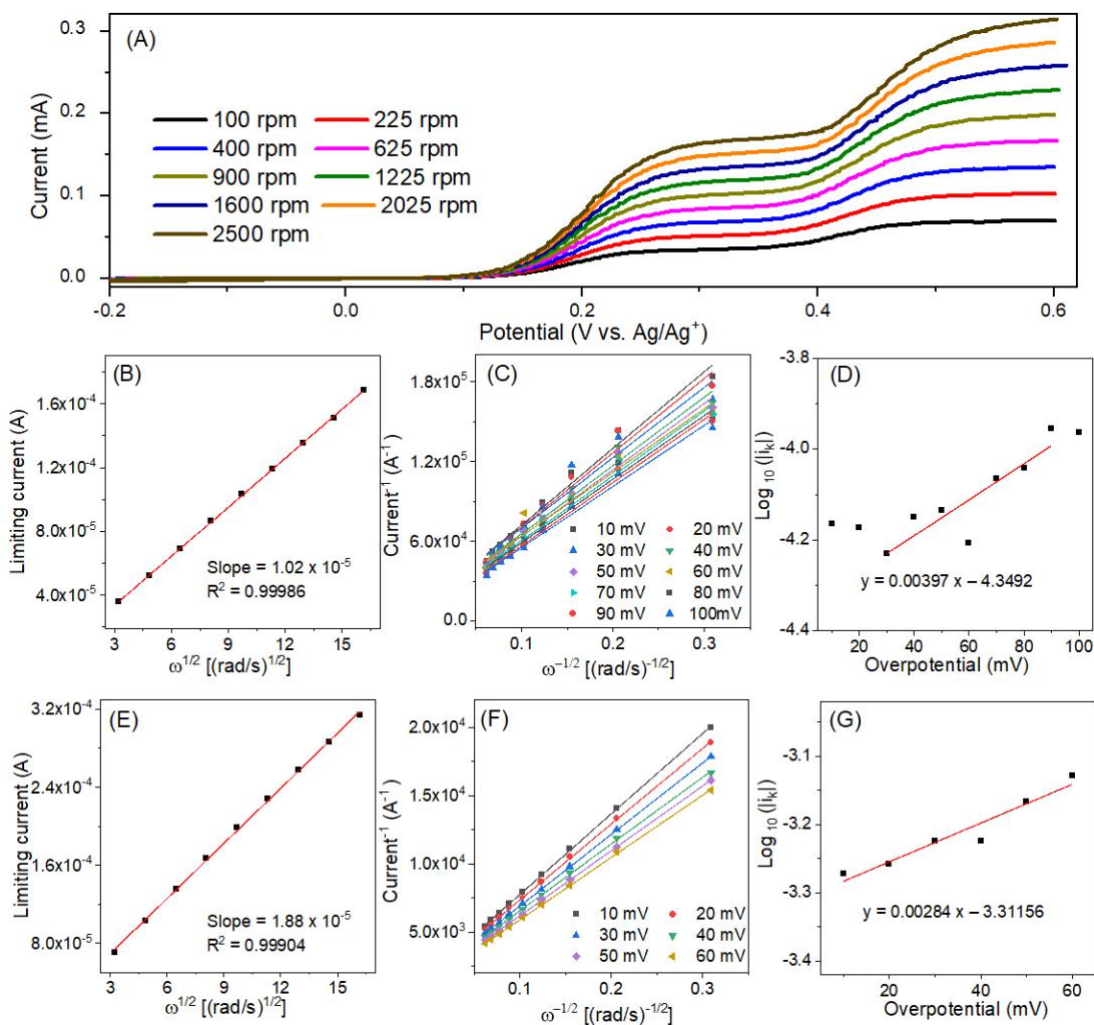
Figure S14. (A) Linear sweep voltammetry plots obtained at different rotation rates of the rotating disk electrode. (B) Peak oxidation and reduction current density versus square root of angular velocity of first electron. (C) Koutecký-Levich curve (current^{-1} vs $\omega^{-1/2}$) at different reduction overpotentials of first electron. (D) Tafel plot constructed using the current response and overpotentials of first electron. (E) Peak oxidation and reduction current density versus square root of angular velocity of second electron. (F) Koutecký-Levich curve (current^{-1} vs $\omega^{-1/2}$) at different reduction overpotentials of second electron. (G) Tafel plot constructed using the current response and overpotentials of second electron. Solution: 1 mM **PEG3-TTF** in a 0.1 M TBAPF$_6$ MeCN solution.
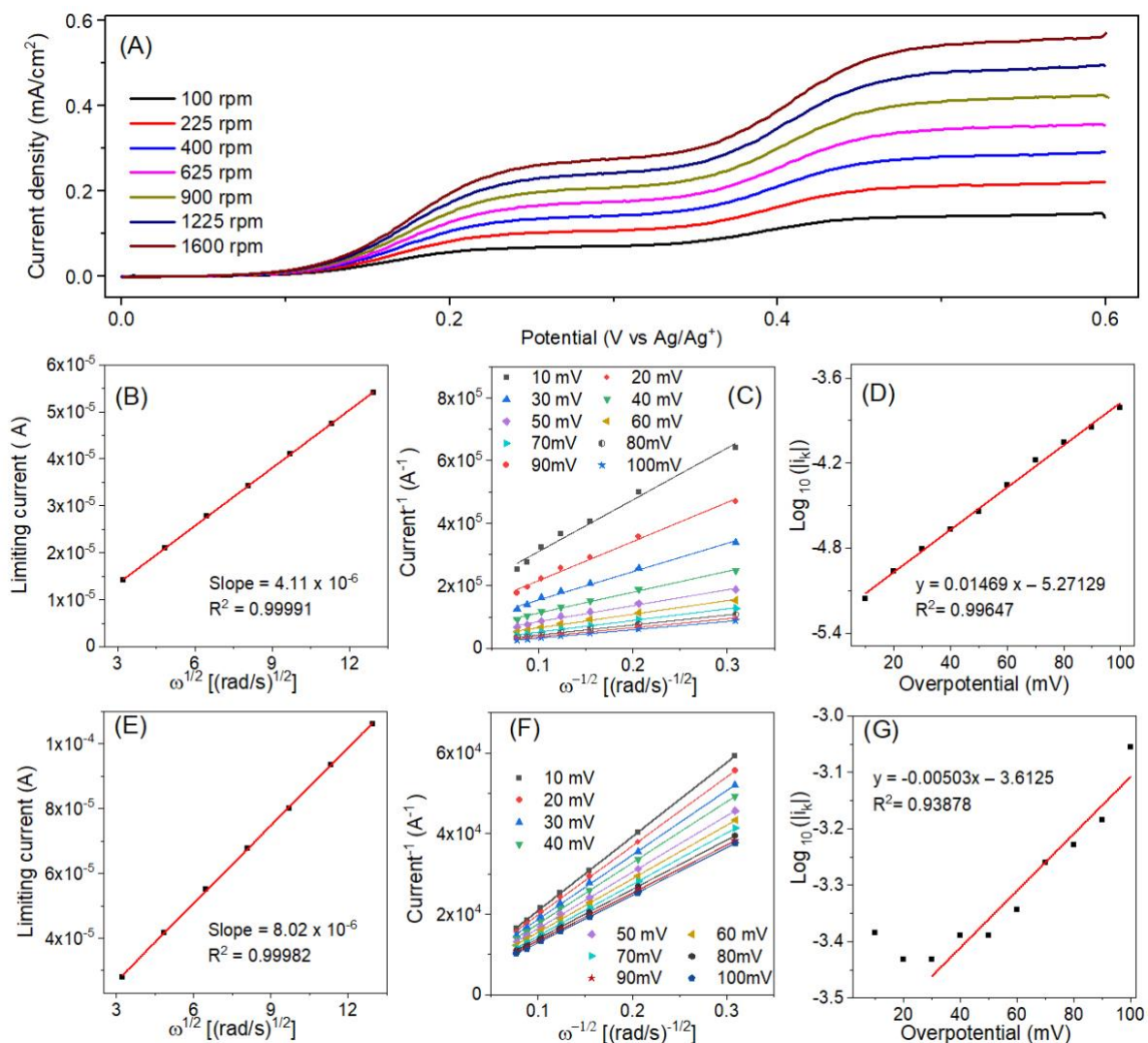
Figure S15. (A) Linear sweep voltammetry plots obtained at different rotation rates of the rotating disk electrode. (B) Peak oxidation and reduction current density versus square root of angular velocity of first electron. (C) Koutecký-Levich curve (current^{-1} vs $\omega^{-1/2}$) at different reduction overpotentials of first electron. (D) Tafel plot constructed using the current response and overpotentials of first electron. (E) Peak oxidation and reduction current density versus square root of angular velocity of second electron. (F) Koutecký-Levich curve (current^{-1} vs $\omega^{-1/2}$) at different reduction overpotentials of second electron. (G) Tafel plot constructed using the current response and overpotentials of second electron. Solution: 1 mM **PEG3-TTF** in a 0.1 M LiPF$_6$-EC/EMC (1:1) solution.

Table S4. Electrokinetic parameters of the **TTF** compounds.

|	Supporting salt and solvent	D_0 (cm^2 s^{-1})	K_0 (cm s^{-1})
1st TTF	0.1 TBAPF$_6$ PC	2.22 x 10^{-5}	4.08 x 10^{-4}
2nd TTF	0.1 TBAPF$_6$ PC	5.72 x 10^{-5}	3.98 x 10^{-3}
1st CN-TTF	0.1 TBAPF$_6$ PC	4.65 x 10^{-6}	2.78 x 10^{-4}
2nd CN-TTF	0.1 TBAPF$_6$ PC	1.31 x 10^{-5}	2.92 x 10^{-3}
1st PEG3-TTF[a]	0.1 TBAPF$_6$ MeCN	6.01 x 10^{-6}	2.37 x 10^{-3}
2nd PEG3-TTF	0.1 TBAPF$_6$ MeCN	1.43 x 10^{-6}	2.58 x 10^{-2}
1st PEG3-TTF[b]	0.1 LiPF$_6$ EC EMC	2.78 x 10^{-6}	2.83 x 10^{-4}
2nd PEG3-TTF	0.1 LiPF$_6$ EC EMC	7.57 x 10^{-6}	1.33 x 10^{-2}
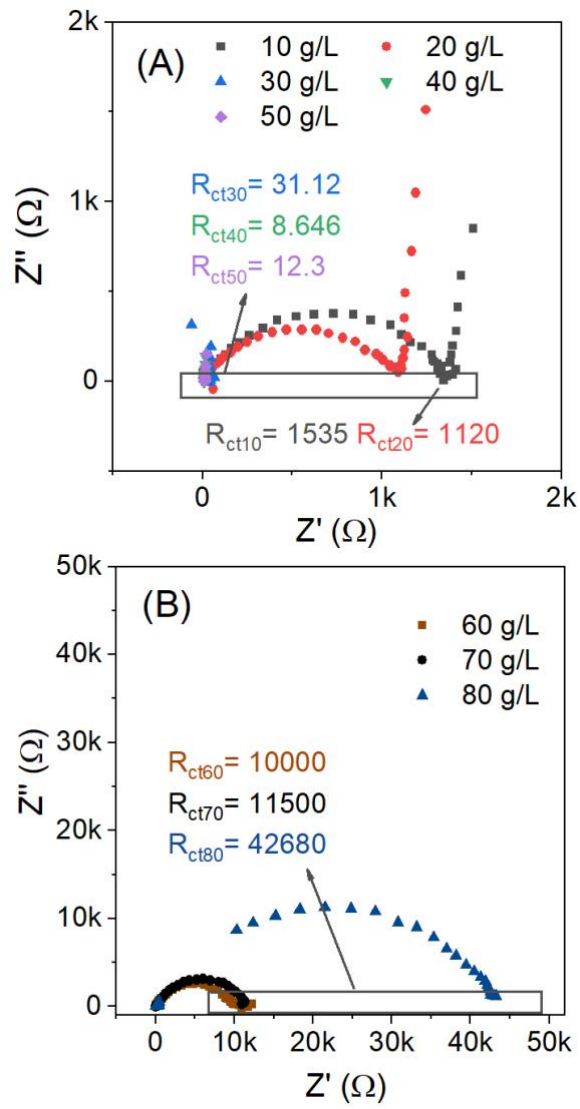
Figure S16. Nyquist profile of three-electrode system with various KB loadings and corresponding R_{ct} values.
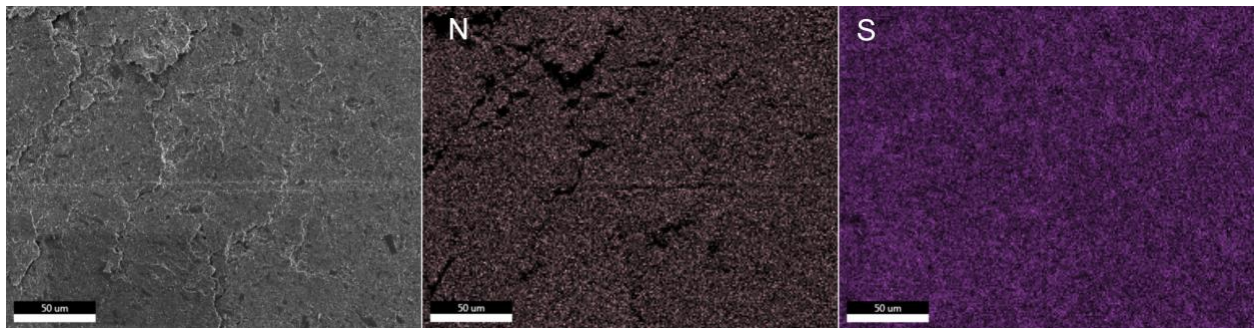
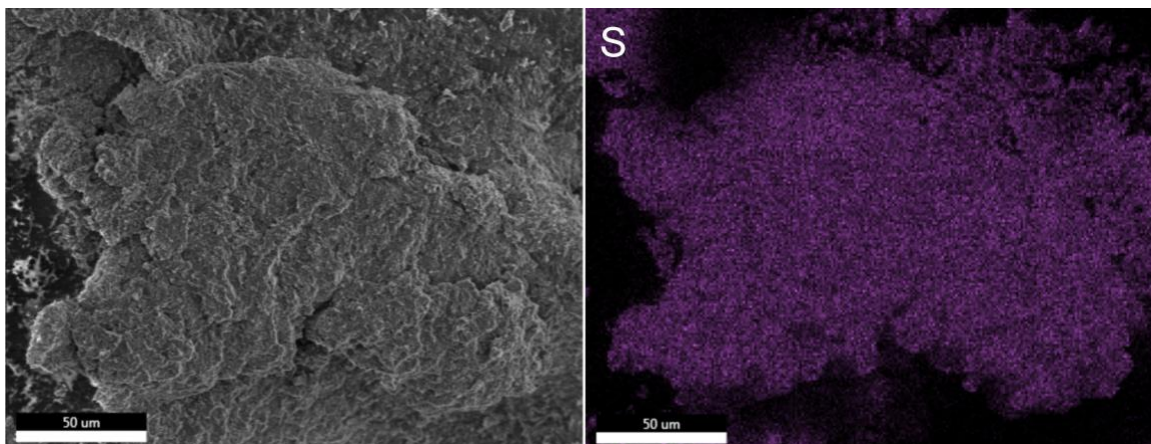

Figure S17. SEM image and element mapping of **CN-TTF**/KB slurry.

Figure S18. SEM image and element mapping of **TTF**/KB slurry.

7. filter paper
8. graphite felt
9. Zn plate

1. PTFE plate
2. copper plate
3. bipolar plate
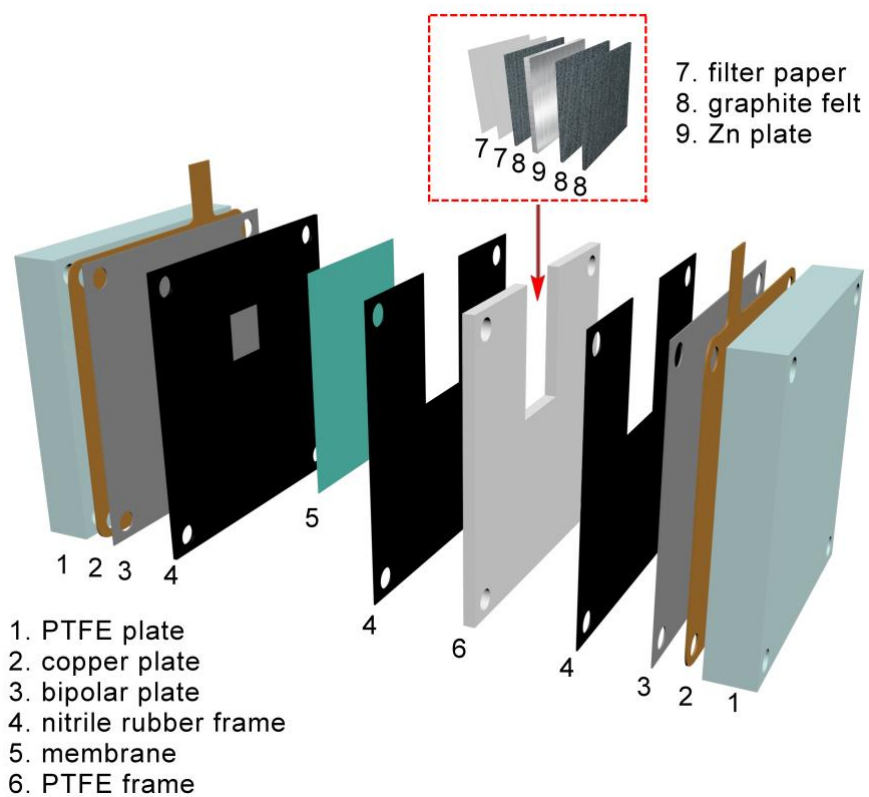4. nitrile rubber frame
5. membrane
6. PTFE frame

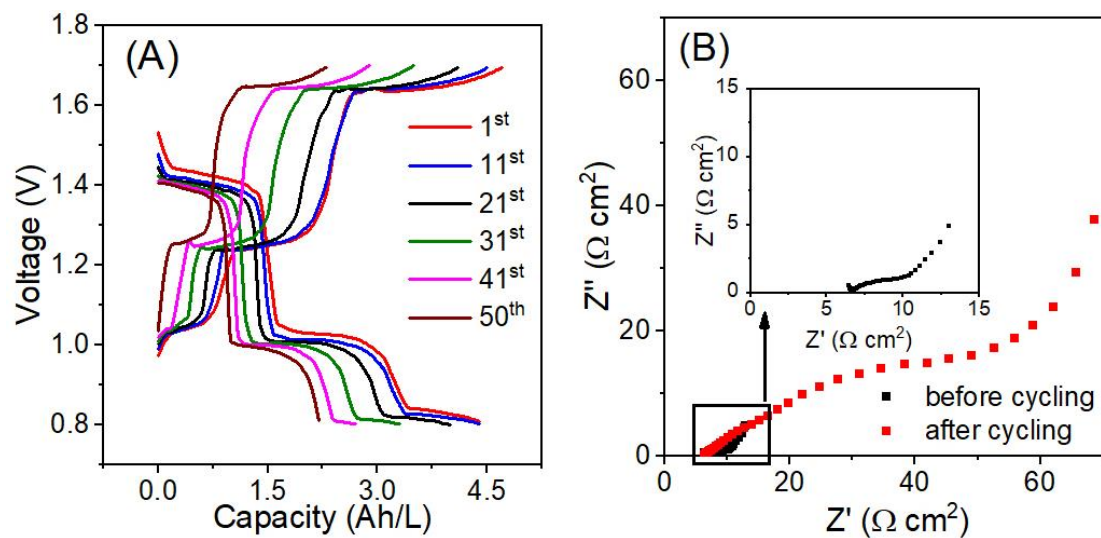**Figure S19.** Schematic diagram of the slurry battery.

Figure S20. (A) Charge/discharge profiles at different cycle numbers of 0.5 M Zn/**TTF** battery. (B) Electrochemical impedance spectroscopy before and after cycling of 0.5 M Zn/**TTF** battery.
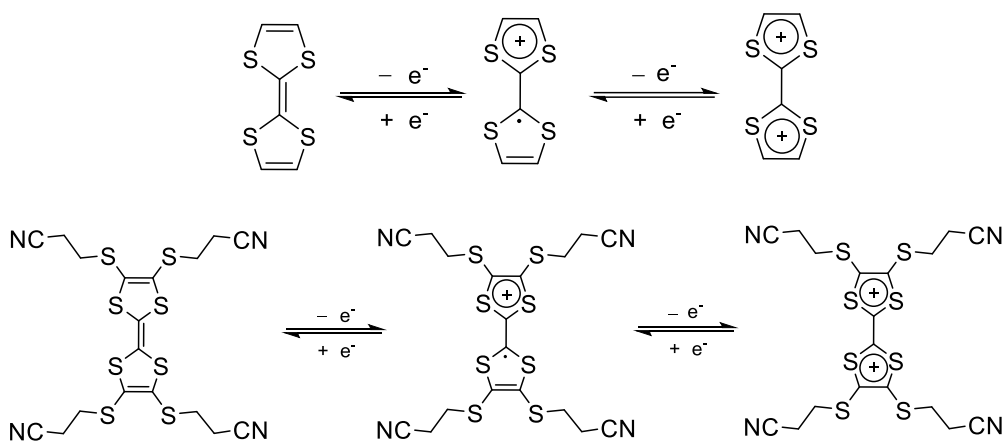

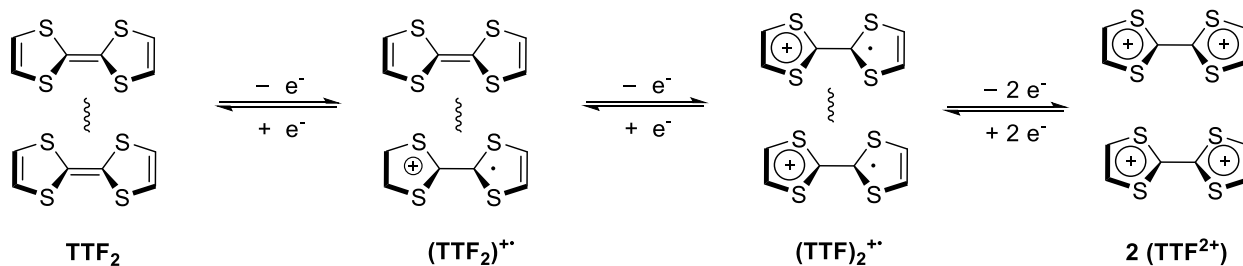**Figure S21.** Redox reactions of **TTF** and **CN-TTF**.

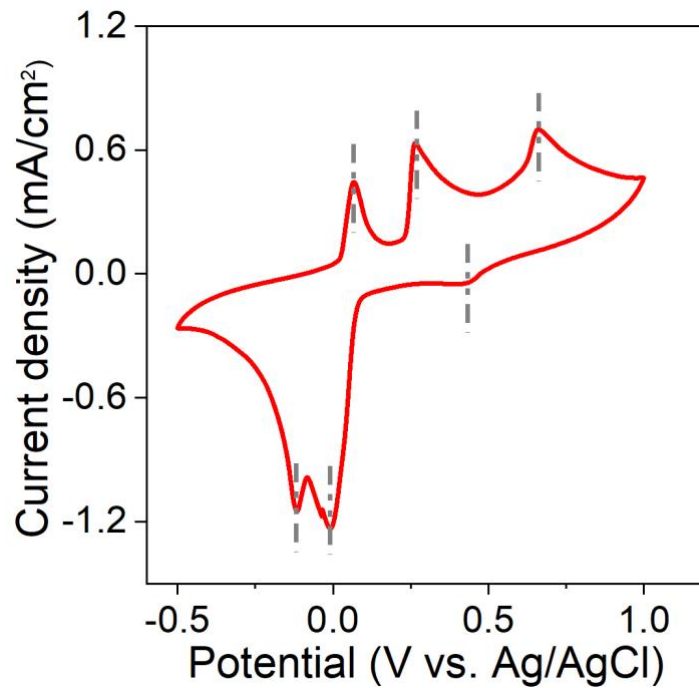**Figure S22.** Dimerization of **TTF**.[S12]

Figure S23. Cyclic voltammograms of deposited **TTF** on carbon paper as working electrode.

Figure S24. Photograph of the dried post-cycling slurry cathode of 0.5 M **TTF** battery.
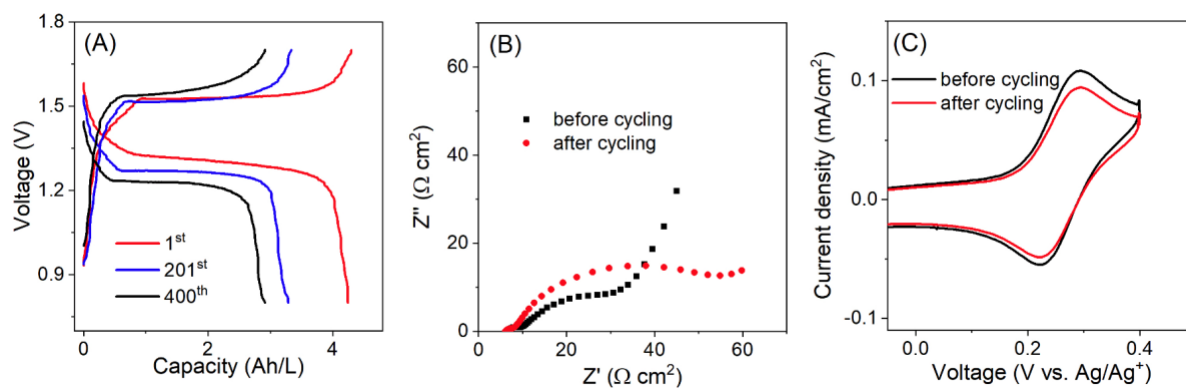
Figure S25. Long cycling properties of the 0.5 M Zn/**CN-TTF** battery. (A) Charge/discharge profiles at different cycle numbers. (B) Electrochemical impedance spectroscopy before and after cycling. (C) CV scans of **CN-TTF** before cycling and after cycling.

Figure S26. The ^{1}H NMR of 0.5 M Zn/**CN-TTF** battery before and after cycling.

Figure S27. The ^{1}H NMR of 1.0 M Zn/**CN-TTF** battery before and after cycling.
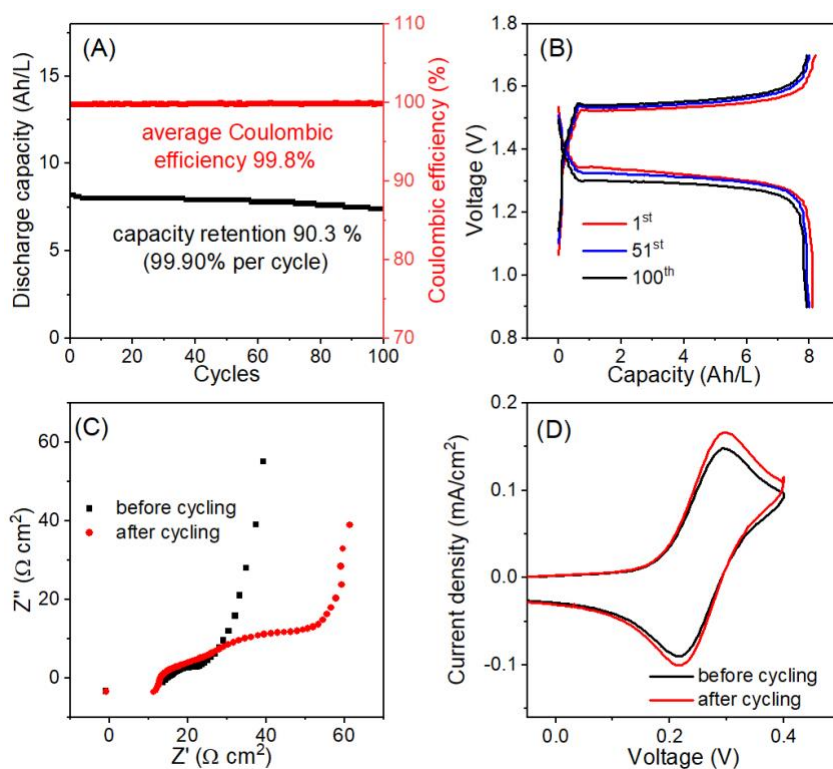
Figure S28. Long cycling properties of 1.5 M Zn/**TTF** battery. (A) Discharge capacity, Coulombic efficiency over 100 cycles. (B) Charge/discharge profiles at different cycle numbers. (C) Electrochemical impedance spectroscopy before and after cycling. (D) CV scans of **CN-TTF** before cycling and after cycling.
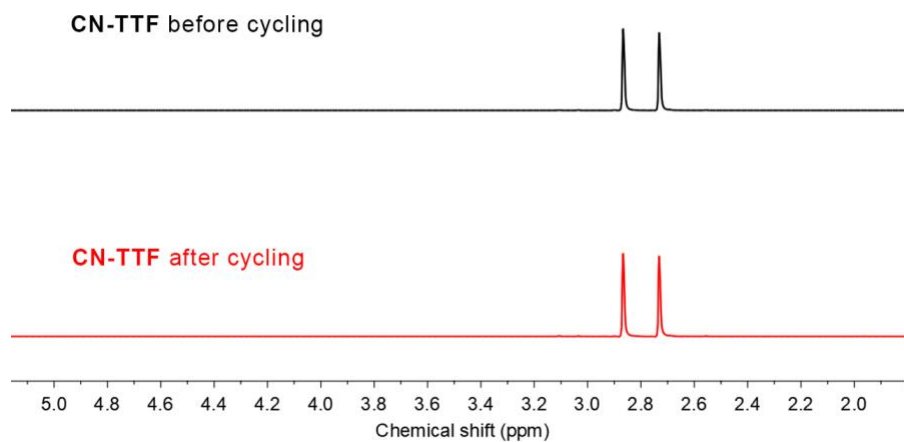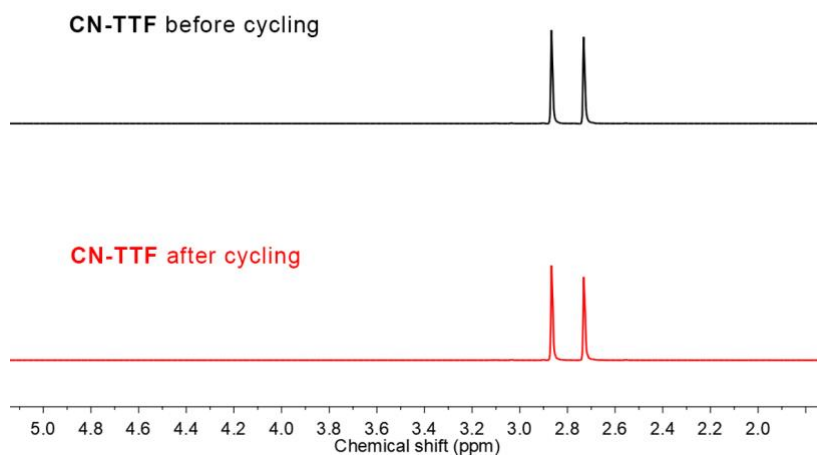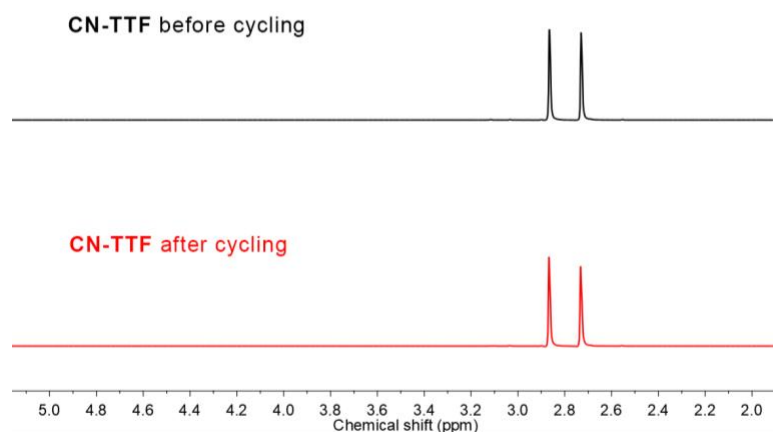
Figure S29. The ^{1}H NMR of 1.5 M Zn/**CN-TTF** battery before and after cycling.
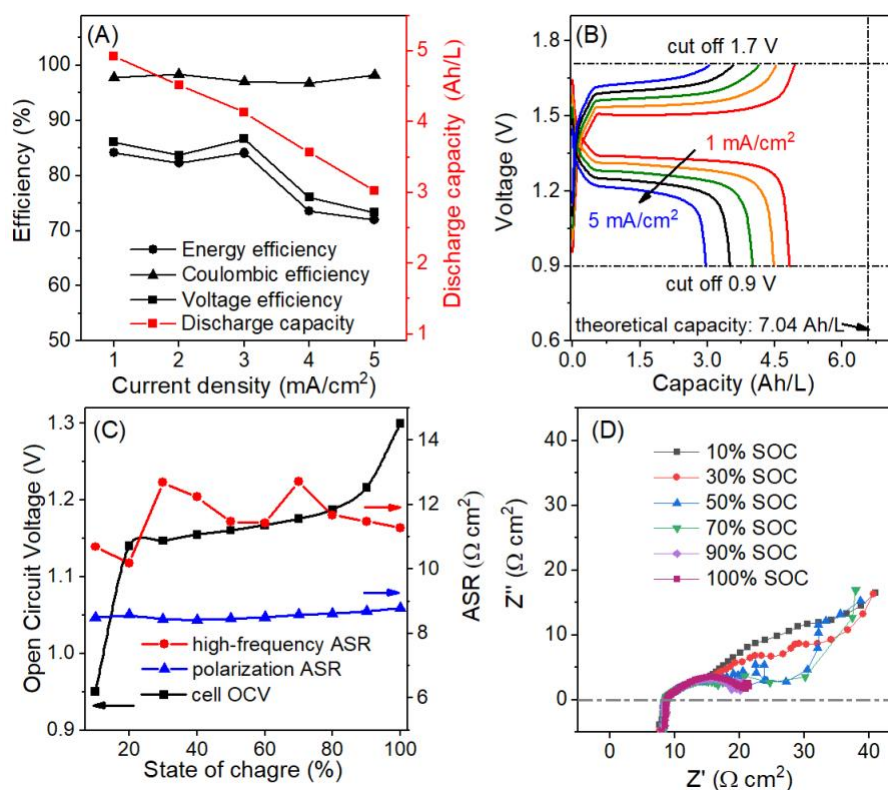
Figure S30. (A) Rate performance of 1.0 M Zn/**CN-TTF** battery: discharge capacity, coulombic efficiency (CE), energy efficiency (EE), and voltage efficiency (VE) at current densities from 1 to 5 mA/cm². (B) Charge/discharge profiles at different current densities. (C) Open-circuit voltage (OCV), high-frequency area specific resistance (ASR), and polarization ASR at different states-of-charge (SOCs). (D) Nyquist impedance of Zn/**CN-TTF** battery at 10, 30, 50, 70, 90, and 100% SOC.
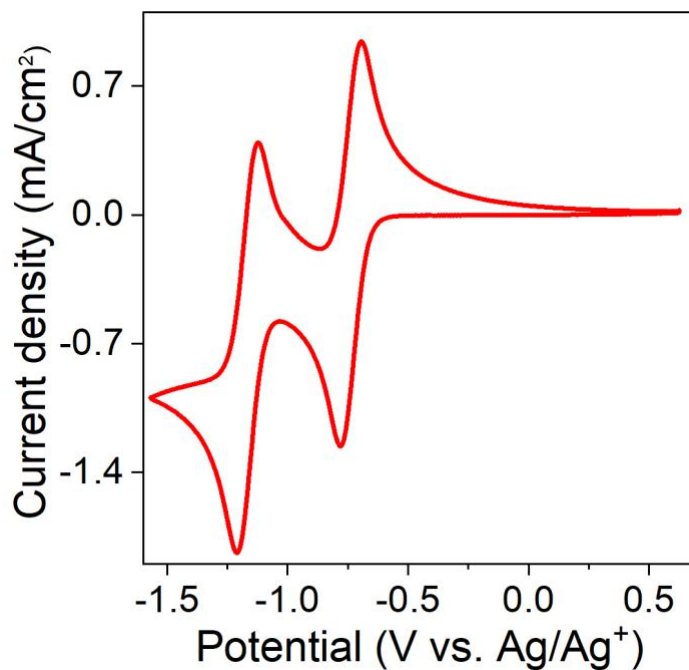
Figure S31. Cyclic voltammograms of **V-TFSI** on 0.1 M TBAPF$_6$ MeCN at scan rate of 50 mV/s.
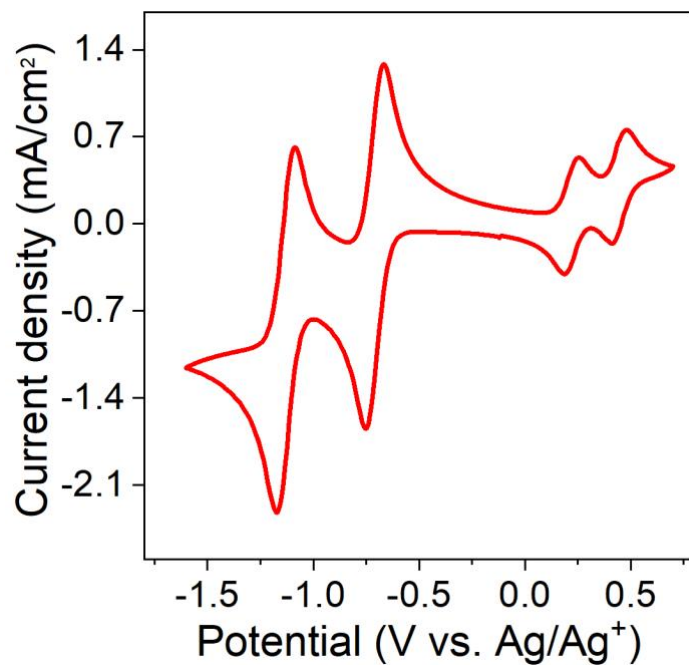
Figure S32. Cyclic voltammograms of 12 mM **V-TFSI** and 5 mM **PEG3-TTF** on 0.1 M TBAPF$_6$ MeCN at scan rate of 50 mV/s.
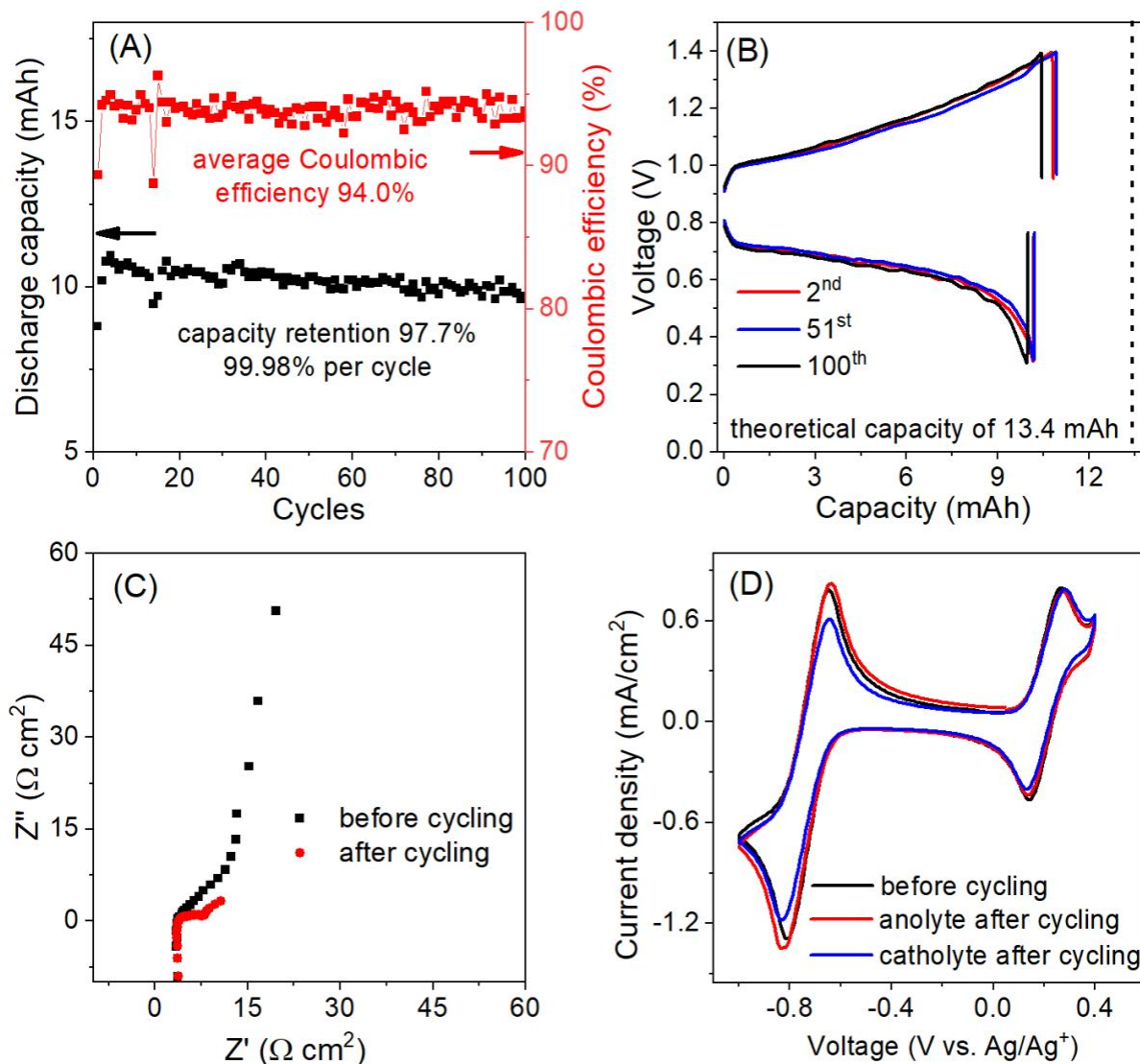
Figure S33. Long cycling properties of the 0.1 M **V-TFSI/PEG3-TTF** single electron battery. (A) Discharge capacity, Coulombic efficiency over 100 cycles. (B) Charge/discharge profiles at different cycle numbers. (C) Electrochemical impedance spectroscopy before and after cycling. (D) CV scans of electrolyte before cycling and after cycling.

Figure S34. Long cycling properties of the 0.1 M Li/**PEG3-TTF** battery. (A) Charge/discharge profiles at different cycle numbers. (B) Electrochemical impedance spectroscopy before and after cycling. (C) CV scans of catholyte before cycling and after cycling. (D) Cyclic voltammograms of post-battery anolyte, condition: scan rate of 50 mV/s, Li as reference electrode.
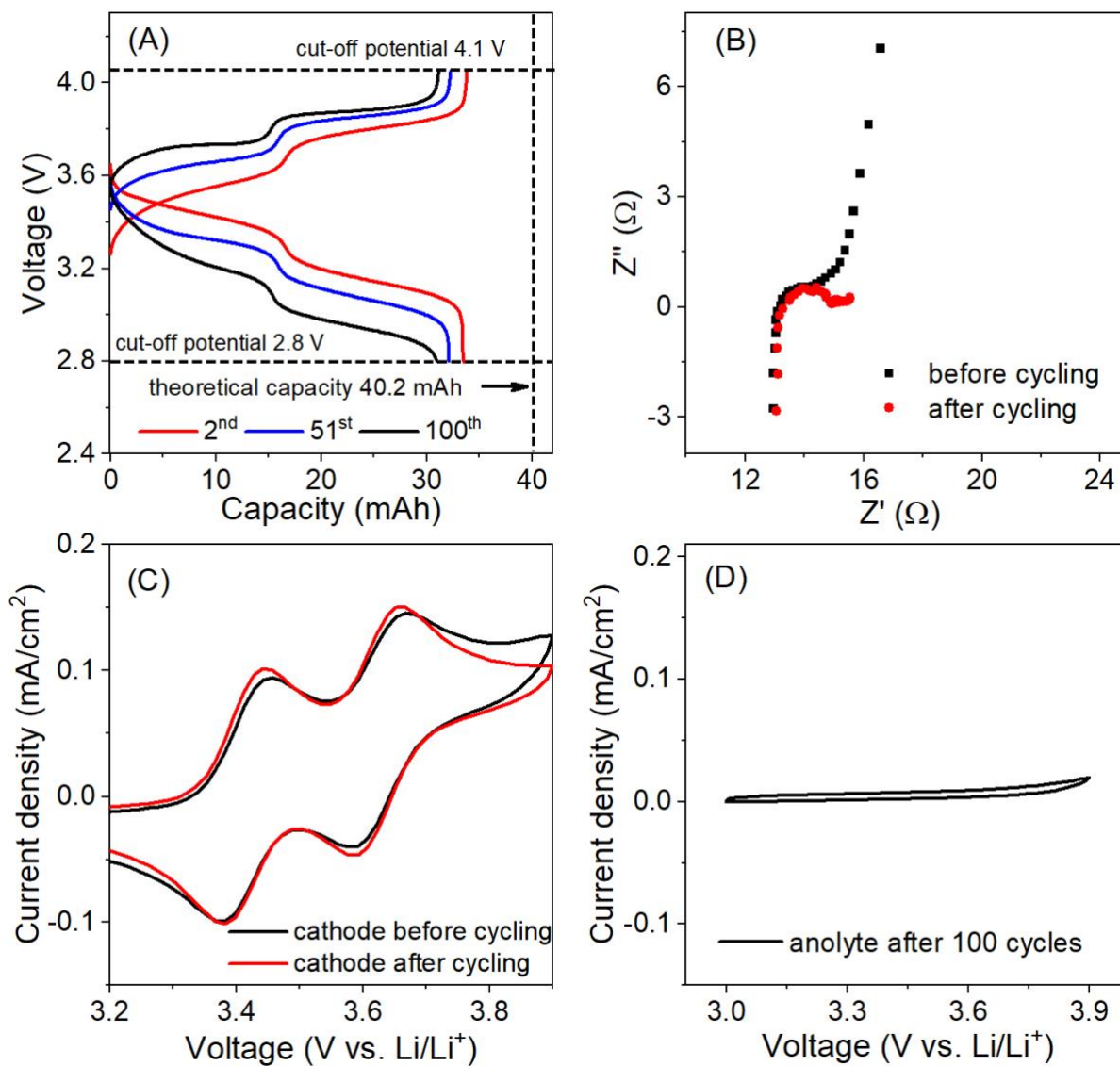
Figure S35. Long cycling properties of the 0.3 M Li/**PEG3-TTF** battery. (A) Charge/discharge profiles at different cycle numbers. (B) Electrochemical impedance spectroscopy before and after cycling. (C) CV scans of catholyte before cycling and after cycling. (D) Cyclic voltammograms of post-battery anolyte, condition: scan rate of 50 mV/s, Li as reference electrode.
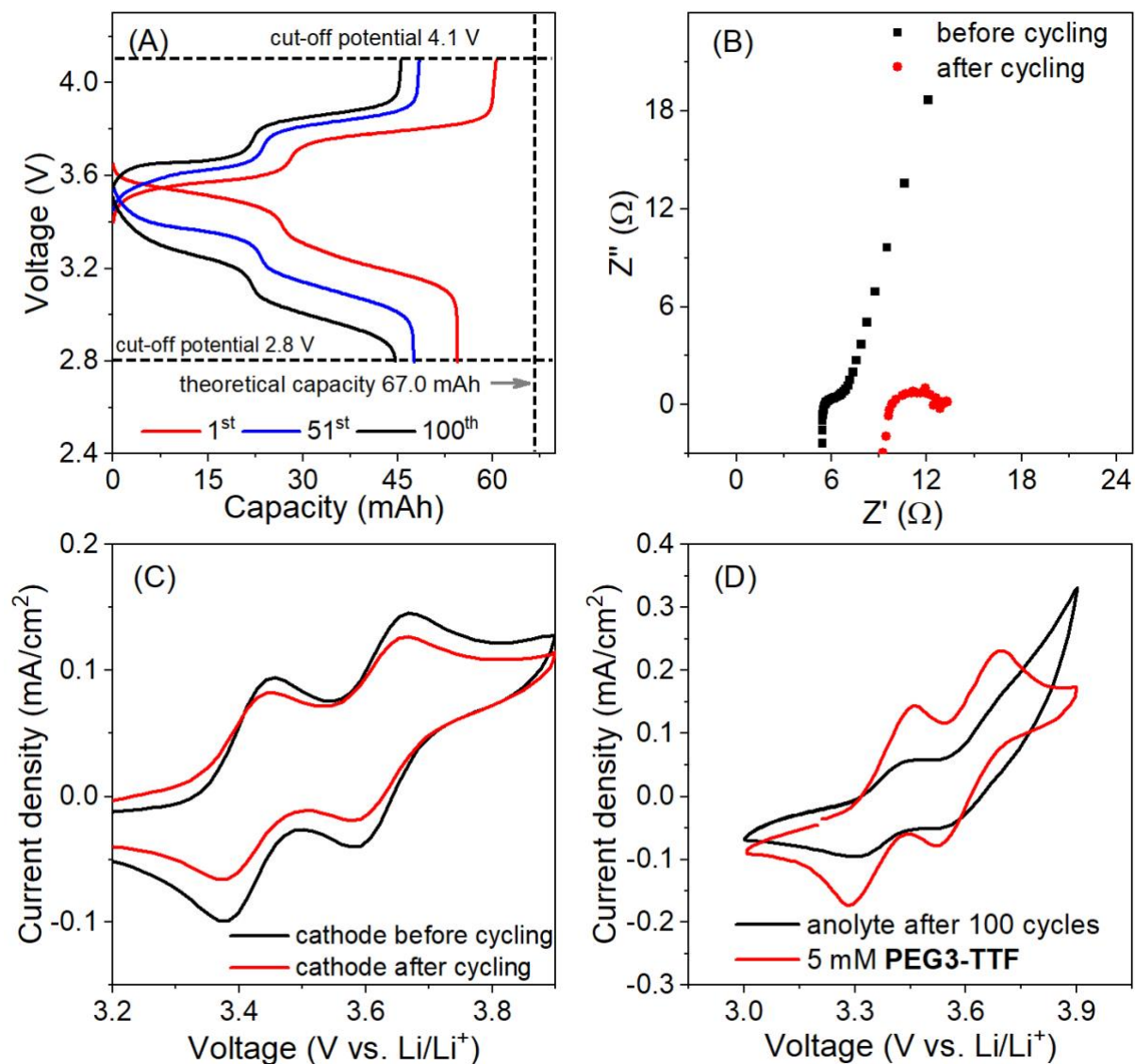
Figure S36. Long cycling properties of the 0.5 M Li/**PEG3-TTF** battery. (A) Charge/discharge profiles at different cycle numbers. (B) Electrochemical impedance spectroscopy before and after cycling. (C) Cyclic voltammogr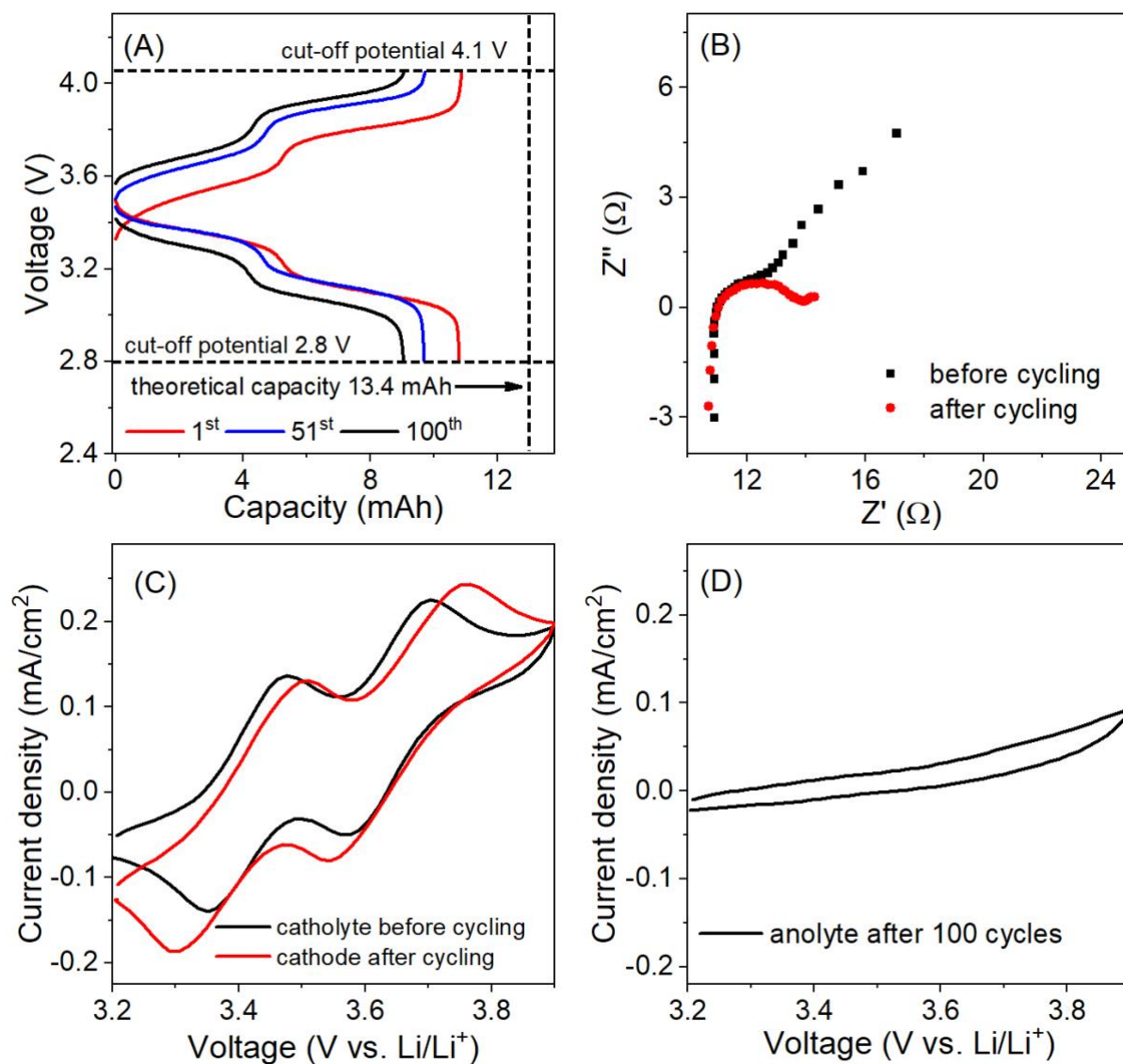ams of catholyte before cycling and after cycling. (D) Cyclic voltammograms of post-battery anolyte, condition: scan rate of 50 mV/s, Li as reference electrode.
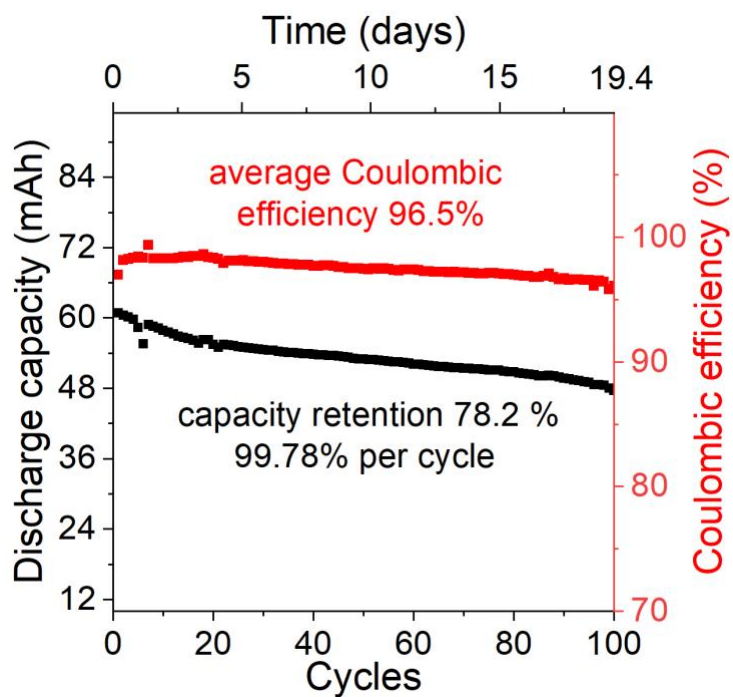
Figure S37. Repeated long cycling properties of the 0.5 M Li/**PEG3-TTF** battery.

Table S5. Summary of cycling performance of the **PEG3-TTF**-based battery.

Anode	Concentration of **PEG3-TTF**	Electron number	Battery potential	Capacity retention	Capacity retention /cycle	Energy density (Wh/L)	Operating time (h)
V-TFSI	0.1 M	1	0.91 V	97.7%	99.98%	1.33	21.2
Li metal	0.1 M	2	3.64 V	88.0%	99.88%	15.29	83.6
Li metal	0.3 M	2	3.64 V	91.7%	99.91%	47.81	268.8
Li metal	0.5 M	2	3.64 V	82.9%	99.83%	88.18	444.2

Table S6. Performance parameters of reported nonaqueous RFBs.

	membrane	Symmetric or asymmetric	Molarity of Electron (M)[a]	Current density (mA/cm²)	Potential (V)	Energy density (Wh/L)[b]	Flow or Static	Operating time (h)
This work	AEM	Asymmetric	0.2	3	3.64	15.29	Flow	84
This work	AEM	Asymmetric	0.6	3	3.64	47.81	Flow	269
This work	AEM	Asymmetric	1.0	3	3.64	88.18	Flow	444
DMFc/Li[S13]	LAGP	Asymmetric	0.05	0.6	~3.1	4	Flow	45
QPT-OMe/Li[S14]	Porous	Symmetric	0.025	30	2.5	0.75	Static	-
TEMPO/Li[S15]	Porous	Symmetric	0.1	5	3.5	7.4	Flow	30
TEMPO-EG1/Li[S16]	Porous	Symmetric	0.1	8	3.54	21.4	Flow	-
NQ/Li[S17]	LATP	Asymmetric	0.1	0.2	~2.8	5.3	Flow	-
FcNTFSI/MVTFSI[S18]	Porous	Symmetric	0.1	30	1.5	24.39	Flow	<20[c]
Fc1N112/Li[S19]	Porous	Symmetric	0.8	3.5	3.49	50	Flow	90
PDI-TEMPO[S20]	AEM	Symmetric	1.0	20	2.22	~4[d]	Flow	-
TETD/Li[S21]	LATP	Asymmetric	2.0	0.3	2.7	125	Static	1000
TETD/Li[S21]	Porous	Symmetric	0.2	10	2.7	~13[d]	Flow	<115[c]
BODMA[S22]	Porous	Asymmetric	0.15	5	4.0	~10	Flow	<60[c]
AQNTFSI/ M FcNTFSI[S23]	Porous	Symmetric	0.2	20	1.72	4.6	Flow	<70[c]
3-Pr/butyl viologen[S24]	Porous	Symmetric	0.05	20	~1.65	2.2[d]	Flow	44
ANL-C46/BzNSN[S25]	Porous	Symmetric	0.1	60	2.67	5.34[d]	Flow	5
Tz-OMe/DBBB[S26]	Porous	Symmetric	0.125	30	~1.85	6.2[d]	Flow	17
PIPEG/Mg[S27]	Nano-porous	Asymmetric	0.5	0.05	1.91	40	Flow	-
AQEGFSI/FcNTFSI[S28]	Porous	Symmetric	0.8	40	1.57	16.8	Flow	<50[c]
NITFSI/FcTFSI[S29]	Porous	Symmetric	1.0	10	~2.0	35.6	Flow	65
MTP/Na[S30]	Na₃Zr₂Si₂PO₁₂	Asymmetric	0.1	1.0	3.58	-	Flow	-
DTDMB/2,3-DMNQ[S31]	Porous	Symmetric	0.2	18	1.85	0.63[d]	Flow	-

[a]Concentration and current density used for long cycling. [b]Operation energy density. [c]Operating time calculation: maximum charging capacity/current×2×cycle numbers. [d]Calculated with Equation S4 using the highest discharge capacity read from literature
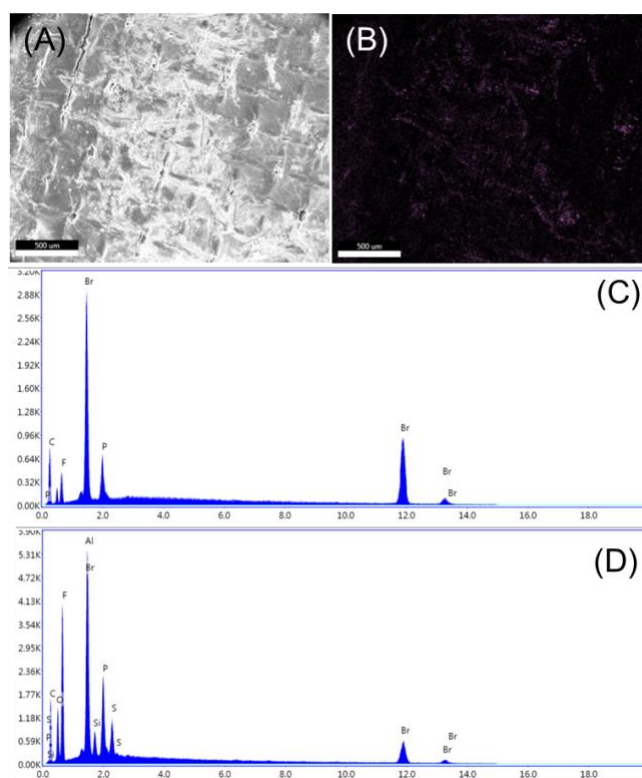
Figure S38. (A) SEM image and element mapping for post-cycling membrane. (B) S element mapping of (A). Elemental species on the membrane before (C) and after (D) cycling.
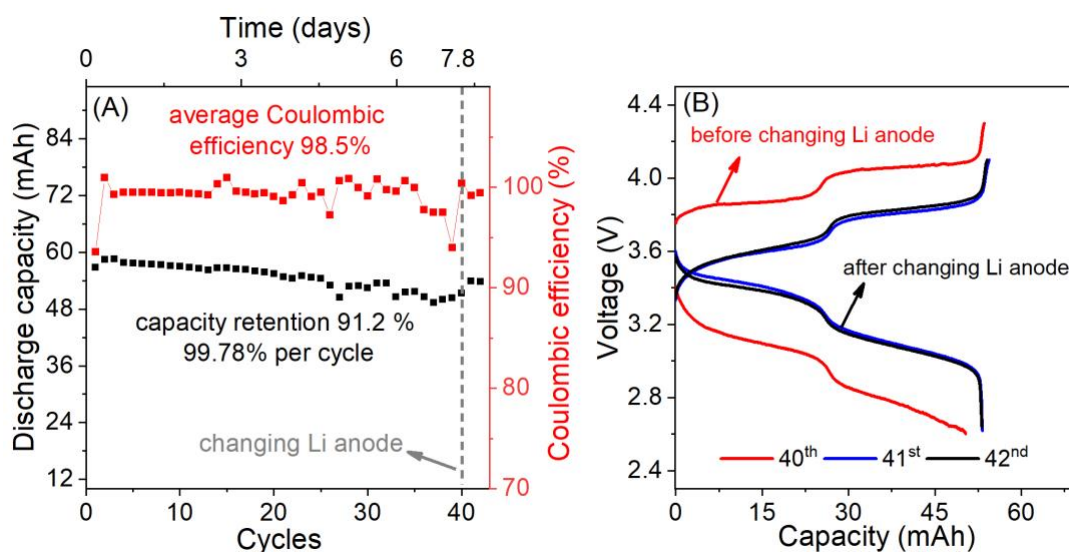
Figure S39. (A) a 40 cycle long cycling properties of the 0.5 M Li/**PEG3-TTF** battery, testing condition: 1-39 cycles 2.8-4.1 V, 3 mA/cm^2, 40-42 cycles 2.6-4.3 V, 3 mA/cm^2 to fully exert capacity. (B)The charge-discharge capacity curve of the battery before and after replacing the negative electrode.
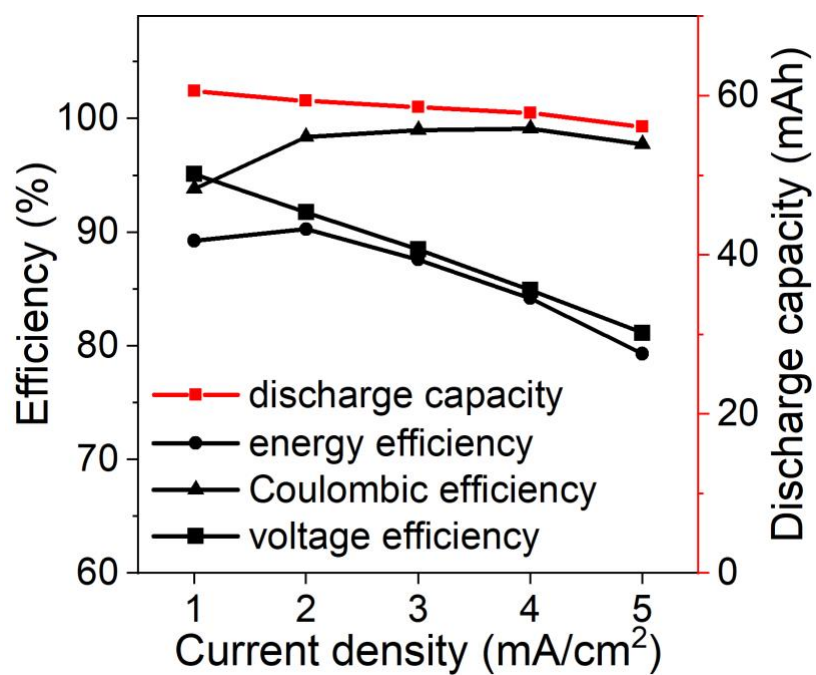
Figure S40. (A) Rate performance of 0.5 M **PEG3-TTF** battery: discharge capacity, coulombic efficiency (CE), energy efficiency (EE), and voltage efficiency (VE) at current densities from 1 to 5 mA/cm^2.
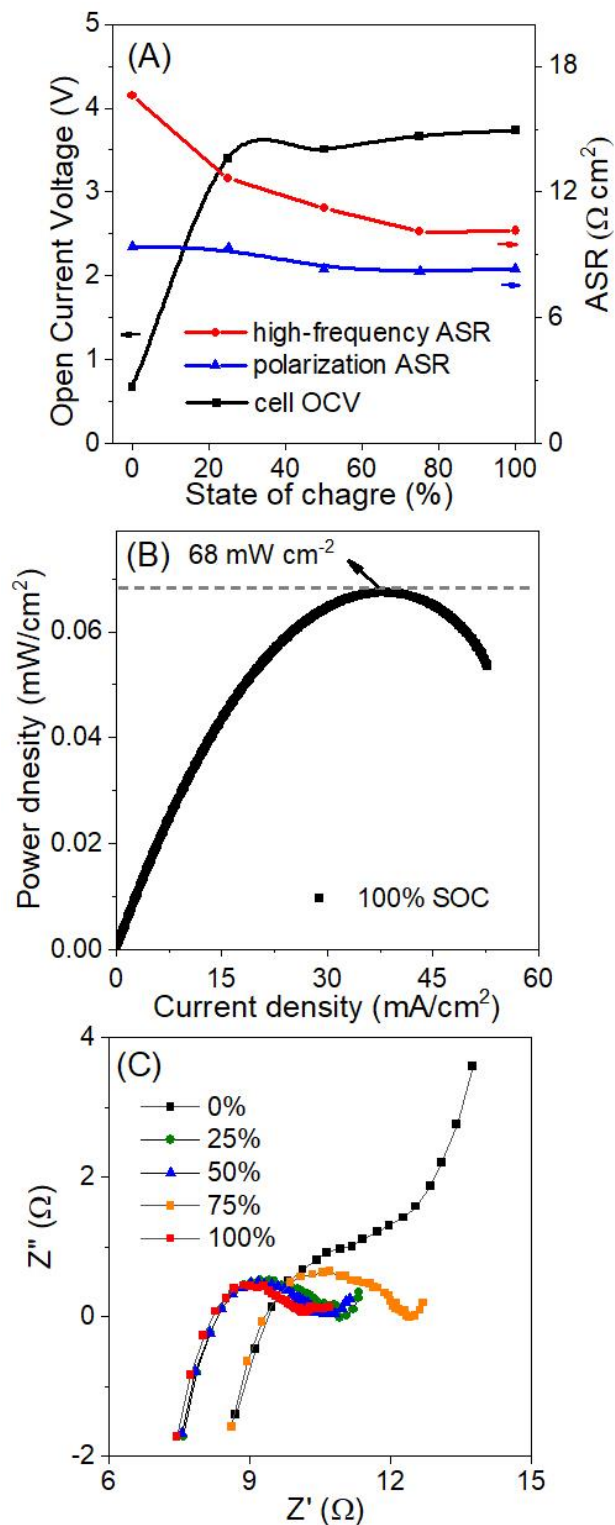
Figure S41. (A) Open-circuit voltage (OCV), high-frequency area specific resistance (ASR), and polarization ASR at different states-of-charge (SOCs). (B) Power density curves for 100% SOC. (C) Nyquist impedance of **PEG3-TTF** battery at 0, 25, 50, 75, and 100% SOC.

Table S7. Performance parameters of reported **TTF** based nonaqueous RFBs.

Work	Role in battery	Concentration of TTF	Battery potential	Capacity retention	Energy density (Wh/L)	Coulombic Efficiency (%)
This one	redoxmer	0.5 M	3.64 V	82.9%	88.18	98.10
Chen[S32]	redoxmer	0.2 M	3.85 V	~48%	~42	91.90
Fujimoto[S33]	redox mediator	0.005 M	3.58 V	NA	NA	NA
Janssen[S34]	redoxmer	0.05 M	~2 V	~50%	~5	99.3

References

S1.   K. Lin, R. Gómez-Bombarelli, E. S. Beh, L. Tong, Q. Chen, A. Valle, A. Aspuru-Guzik, M. J. Aziz and R. G. Gordon, *Nat. Energy*, 2016, **1**, 16102.

S2.   E. S. Beh, D. De Porcellinis, R. L. Gracia, K. T. Xia, R. G. Gordon and M. J. Aziz, *ACS Energy Lett.*, 2017, **2**, 639–644.

S3.   B. Hu, C. DeBruler, Z. Rhodes and T. L. Liu, *J. Am. Chem. Soc.*, 2017, **139**, 1207–1214.

S4.   Y. Ding, Y. Zhao, Y. Li, J. B. Goodenough and G. Yu, *Energy Environ. Sci.*, 2017, **10**, 491–497.

S5.   J. Zhang, G. Jiang, P. Xu, A. Ghorbani Kashkooli, M. Mousavi, A. Yu and Z. Chen, *Energy Environ. Sci.*, 2018, **11**, 2010–2015.

S6.   C. DeBruler, B. Hu, J. Moss, X. Liu, J. Luo, Y. Sun and T. L. Liu, *Chem*, 2017, **3**, 961–978.

S7.   N. Svenstrup, K. M. Rasmussen, T. K. Hansen and J. Becher, *Synthesis*, 1994, **1994**, 809–812.

S8.   C. S. Velázquez and R. W. Murray, *J. Electroanal. Chem.*, 1995, **396**, 349–357.

S9.   M. Dekhtiarenko, M. Allain, V. Carré, F. Aubriet, Z. Voitenko, M. Sallé and S. Goeb, *New J. Chem.*, 2021, **45**, 21015–21019.

S10.   J. Lyskawa, F. Le Derf, E. Levillain, M. Mazari and M. Sallé, *EurJOC*, 2006, **2006**, 2322–2328.

S11.   M. Shao, P. Dongare, L. N. Dawe, D. W. Thompson and Y. Zhao, *Org. Lett.*, 2010, **12**, 3050–3053.

S12.   M. Hasegawa and M. Iyoda, *Organic Redox Systems: Synthesis, Properties, and Applications,(Ed.: T. Nishinaga), Wiley*, 2015, 89–125.

S13.   G. Cong, Y. Zhou, Z. Li and Y.-C. Lu, *ACS Energy Lett.*, 2017, **2**, 869–875.

S14.   Y. Liu, G. Dai, Y. Chen, R. Wang, H. Li, X. Shi, X. Zhang, Y. Xu and Y. Zhao, *ACS Energy Lett.*, 2022, 1274–1283.

S15.   X. Wei, W. Xu, M. Vijayakumar, L. Cosimbescu, T. Liu, V. Sprenkle and W. Wang, *Adv. Mater.*, 2014, **26**, 7649–7653.

S16.   Y. Zhao, J. Zhang, G. Agarwal, Z. Yu, R. E. Corman, Y. Wang, L. A. Robertson, Z. Shi, H. A. Doan, R. H. Ewoldt, I. A. Shkrob, R. S. Assary, L. Cheng, V. Srinivasan, S. J. Babinec and L. Zhang, *J. Mater. Chem. A*, 2021, **9**, 16769–16775.

S17.   Y. Ding, Y. Li and G. Yu, *Chem*, 2016, **1**, 790–801.

S18.   B. Hu and T. L. Liu, *J. Energy Chem.*, 2018, **27**, 1326–1332.

S19.   X. Wei, L. Cosimbescu, W. Xu, J. Z. Hu, M. Vijayakumar, J. Feng, M. Y. Hu, X. Deng, J. Xiao, J. Liu, V. Sprenkle and W. Wang, *Adv. Energy Mater.*, 2015, **5**, 1400678.

S20.   G. S. Nambafu, E. P. Delmo, U. Bin Shahid, C. Zhang, Q. Chen, T. Zhao, P. Gao, K. Amine and M. Shao, *Nano Energy*, 2022, **94**, 106963.

S21.   L. Zhang, B. Zhao, C. Zhang and G. Yu, *Angew. Chem. Int. Ed.*, 2021, **60**, 4322–4328.

S22.   J. Zhang, Z. Yang, I. A. Shkrob, R. S. Assary, S. o. Tung, B. Silcox, W. Duan, J. Zhang, C. C. Su, B. Hu, B. Pan, C. Liao, Z. Zhang, W. Wang, L. A. Curtiss, L. T. Thompson, X. Wei and L. Zhang, *Adv. Energy Mater.*, 2017, **7**, 1701272.

S23.   Y. Zhen, C. Zhang, J. Yuan and Y. Li, *J. Mater. Chem. A*, 2021, **9**, 22056–22063.

S24.   Y. Yan, R. Walser-Kuntz and M. S. Sanford, *ACS Mater. Lett.*, 2022, DOI: 10.1021/acsmaterialslett.2c00050, 733–739.

S25.   S. R. Bheemireddy, Z. Li, J. Zhang, G. Agarwal, L. A. Robertson, I. A. Shkrob, R. S. Assary, Z. Zhang, X. Wei, L. Cheng and L. Zhang, *ACS Appl. Mater. Interfaces*, 2022, **14**, 28834–28841.

S26.   G. D. De La Garza, A. P. Kaur, I. A. Shkrob, L. A. Robertson, S. A. Odom and A. J. McNeil, *J. Mater. Chem. A*, 2022, DOI: 10.1039/d2ta04515j.

S27.   Y. Qin, K. Holguin, D. Fehlau, C. Luo and T. Gao, *ACS Appl. Energy Mater.*, 2022, **5**, 2675–2678.

S28.   Y. Zhen, C. Zhang and Y. Li, *ACS Appl. Mater. Interfaces*, 2022, **14**, 17369-17377.

S29.   D. Xu, C. Zhang and Y. Li, *Chem. Eng. J.*, 2022, **439**.

S30.   X. Yu and A. Manthiram, *Energy Storage*, 2021, **4**.

S31.   P. Vallayil, K. Ramanujam and S. Sankararaman, *Electrochim. Acta*, 2022, **407**.

S32.   W. Hu, J. Xu, N. Chen, Z. Deng, Y. Lai and D. Chen, *Green Energy Environ.*, 2022, DOI: 10.1016/j.gee.2022.10.005.

S33.   H. Nariyama, S. Ito, Y. Okada, Y. Inatomi, K. Ichikawa, Y. Masumoto and M. Fujimoto, *Electrochim. Acta*, 2022, **409**, 139915.

S34.   N. Daub, K. H. Hendriks and R. A. J. Janssen, *Batter. Supercaps*, 2022, **5**, e202200386.